Modelling a High Precision Fibre Optic Gyroscope for Low-frequency Active Seismic Isolation Université de Liège

Auteur : Sánchez Soler, Alejandro
Promoteur(s) : Collette, Christophe
Faculté : Faculté des Sciences appliquées
Diplôme : Master en ingénieur civil en aérospatiale, à finalité spécialisée en "aerospace engineering"
Année académique : 2025-2026
URI/URL : http://hdl.handle.net/2268.2/26128

UNIVERSITE DE LIEGE
FACULTE DES SCIENCES APPLIQUEES

Modelling a High Precision Fibre Optic Gyroscope for Low-frequency Active Seismic Isolation

Sánchez Soler Alejandro

Thesis presented to obtain the degree of :

Master of Science in Aerospace Engineering

Thesis supervisor :

Collette Christophe

Academic year: **2025 - 2026**

Acknowledgments

This work represents the end of a completely new experience that has lasted for two years. During this period I have gone through many little and even some big journeys, from which I'm grateful for being now part of me. Every opportunity might not look like a gift, but is on someone to make the best of it.

This work is one more journey but represents the end of many other that have happened during these two years. Therefore, I would like to thank...

My family for always supporting me and making me grateful of being back home, specially to my mother and my sister, which have been present at each step of my journey, accompanying me with their warmth,

My friends in Almería for keeping me busy with the same things we love ever since I know them.

My friends from the bachelor in Madrid for being the smartest dumbest people I know (alongside me, of course), specially the ones in Netherlands, for being an oasis for occasional scapes and zoom out,

All the people and friends I've met during my two years in Liège, the ones who came and went and the few who stayed. They have filled this time with a lot of good, bad and unforgettable memories,

My colleagues from the PML and Christophe, specially Annalisa and Hemendra for being that kind and continuous support throughout the day, and Tibú for teaching and guiding me,

My best friend for being that one I could be in a deserted island with and turn it into a paradise, and for being always there for me,

Finally, to everyone who has ever given me a true smile from the heart. For sure I returned it back, in hope that they feel my gratitude, for them to smile purely again.

Summary

The next-generation Einstein Telescope (ET) requires unprecedented low-frequency active seismic isolation to broaden the observable spectrum of gravitational waves towards low frequencies. A fundamental limitation in achieving this is the tilt-horizontal coupling experienced by standard inertial sensors, which causes rotation to produce an undistinguishable signal from horizontal translation. This requires the development of a dedicated, highly sensitive rotation sensor capable of reaching a noise floor of 10^{-10} rad/s/$\sqrt{\text{Hz}}$ in the critical 10 mHz to 10 Hz bandwidth.

This thesis investigates the design and theoretical evaluation of a custom high-precision Fibre Optic Gyroscope (FOG) to meet these demanding requirements. The FOG, based on the Sagnac effect, was selected over mechanical beam balances and Ring Laser Gyroscopes (RLG) due to its flat transfer function from DC, inherent insensitivity to translational motion, and structural flexibility.

The study presents a progressive architectural evolution from a simple interferometer to an increasingly complex and refined configuration. A comprehensive theoretical noise budget is developed at the beginning, systematically identifying and mitigating both fundamental and environmental noise sources. Key design implementations include a broadband Amplified Spontaneous Emission (ASE) source to suppress Coherent Rayleigh Backscattering (CRB) and the Optical Kerr Effect; a Multifunction Integrated Optical Chip (MIOC) to handle precise 50/50 splitting, polarization, and $\pi/2$ phase modulation; and Lyot depolarisers to mitigate polarization cross-coupling and fading. To address environmental perturbations, a quadrupole winding pattern is applied to geometrically cancel the thermal Shupe effect and acousto-optic noise, while a μ-metal enclosure mitigates the Faraday effect. Furthermore, a large-scale sensing coil ($D = 2.5$ m, $L = 20$ km) is modelled to maximize the Sagnac scale factor (K_S), alongside an active Relative Intensity Noise (RIN) subtraction scheme.

The theoretical evaluation of the final sensor architecture exhibits a noise floor of approximately 10^{-6} rad/s/$\sqrt{\text{Hz}}$, predominantly limited by residual RIN and CRB. Although this performance falls four orders of magnitude short of the strict ET target, it already displays a significant improvement and demonstrated compared to the initial configuration. Ultimately, this thesis validates the potential of the large-scale custom FOG approach, providing a meticulously detailed theoretical foundation, identifying the dominant limiting factors, and establishing a clear engineering roadmap for future experimental development and optimization.

Contents

List of Figures

List of Tables

Chapter 1

Introduction

Gravitational wave detection is constantly progressing towards more advanced instruments to broaden the span of events and time these events can be detected and recorded. However, fostering this progress requires expertise across every technical domain that comprises a gravitational wave detector, such as cryogenics, Newtonian noise, thermal analysis, active isolation or low-frequency vibration sensing. Regarding this thesis, the work has focused on pushing advances in techniques to measure tilt at low frequencies for actively isolating the corresponding platforms of the Einstein Telescope (ET).

The purpose of the Einstein Telescope is to measure gravitational waves in a broader range than the previous detectors, detecting new types of events and at earlier stages by extending the operational bandwidth and improving low-frequency resolution respectively. However, to understand better the purpose and the challenges that face gravitational wave detectors, first is convenient to walk through the physical phenomena that give to them meaning.

1.1 Gravitational Waves

Gravitational waves are a astronomical phenomena product of the movement in spacetime of objects with mass. Nevertheless, it is only possible to detect the most massive events in space by the technology human kind possesses to this day, from the merge of neutron stars to the merge of black holes.

The start of gravitational waves theory dates of 1915 with the formulation of General Relativity by Albert Einstein [21]. It completely changes the perception of how gravity is conceived, from an instantaneous and localized force acting across a distance, to a geometric curvature in the fabric of time and space driven by mass and energy as shown in figure 1.1. One year later, he derived the existence of gravitational waves as an intrinsic consequence of his theory.

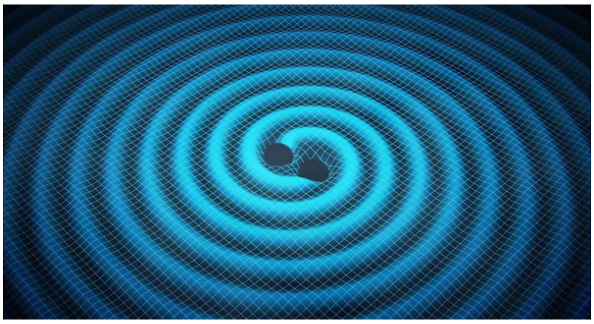

Figure 1.1: Generation of gravitational waves scheme through a Binary Black Hole (BBH) merger [1].

When two celestial bodies become mutually bound by their gravitational attraction, they form a binary system and enter an in-spiral phase. During this process, the bodies orbit one another while gradually drawing closer together, eventually merging into a single object. This phenomenon, known as a compact binary coalescence, is the most frequently detected event. Binary Black Holes (BBH) mergers are generally the strongest sources in this category, since they are the most massive compact bodies in the universe. As well, Binary Neutron Stars (BNS) produce weaker gravitational signals but they are also of significant interest for emitting electromagnetic radiation across a broad spectrum, characterizing them as multimessenger events.

On parallel, there are other 3 events which generate gravitational waves across the universe [21].

- Continuous Gravitational Waves. They produce nearly monochromatic signals which are expected to come from rapidly-spinning neutron stars (pulsars). Signals stay constant along big astronomical time scales, but their signal is too small to be detected by current GWD.
- Stochastic Gravitational Wave Background (SGWB). It consists of a superposition of numerous unresolved signals that manifest as a pervasive noise floor.. Expectations rely on diverse sources dating back to the origin of the universe, which still lingers in space nowadays.
- Burst Sources. Represents punctual bursts of gravitational waves generated by fast transitions between two states with significantly different mass. Generally, these are caused by core-collapse supernovas or other not profoundly understood events in the universe.

Gravitational waves consists on ripples in the fabric of space-time that squeeze and stretch matter over an oscillation. It occurs in two different axis, the plus and cross polarizations, which are orientated 45° apart from each other, as seen in figure 1.2. It is a transverse wave, meaning that it propagates along one axis but the deformation occurs in the orthogonal plane. However, due the immense distance that separates the solar system from these events and the stiffness of the spacetime fabric, the amplitude of the perturbations are incredibly small. Considering a typical event like two black holes merging millions of light years away, the strain of the waves are in the order of 10^{-21} $[\frac{m}{m}]$. To put in context this magnitude, a strain of such size over 1 kilometre would be equivalent to a stretch as small as the millesimal fraction of a proton diameter approximately.

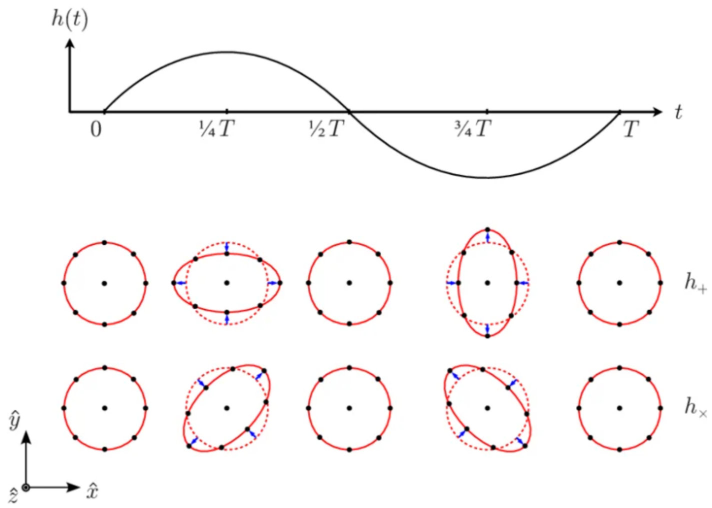

Figure 1.2: Gravitational wave physical perturbation over a period. Plus and cross components [2].

Since gravitational waves are ripples in spacetime that induce a strain, they are extremely difficult to detect with traditional mechanical inertial sensors. Therefore, modern observatories use light interferometry to measure the tiny changes in the optical path length. Consequently, inside the gravitational wave detectors, it is created a controlled environment for light to travel, so when a gravitational wave crosses the detector, the distance that light travels changes, producing a different pattern of interference that is measured. The later technology are interferometers, and they are often used in all corners of the industry.

1.2 Gravitational Waves Detectors

Even though Einstein theoretically predicted gravitationally waves in 1916, their direct detection would not come until almost a century later. However, in 1974 their existence were indirectly evidenced by Hulse and Taylor, proving through radio observations, that the orbital period of a binary system was decaying in perfect agreement with Einstein's equations due to gravitational wave emissions. Over 40 years later, in 2015 the Advanced LIGO detectors registered simultaneously a signal, consistent with a Binary Black Hole system of around 30 solar masses each and 4 months later they officially announced the discovery, representing the culmination of decades of technological development and scientific work [21].

Currently, there exists 3 gravitational wave detectors (GWD) in the world: the Advanced LIGO in United States, the advanced VIRGO in Italy and the KAGRA in Japan, Together they form a global network which have more than 200 hundred potential phenomena registered and rely on the same measurement principle. [22]These are kilometric Michelson interferometers, improved with Fabry-Pérot optical cavities and high sophistication.

The architecture of these modern interferometric detector use highly stabilized and high power laser that is split into two beams which travel back and forth a linear path as depicted in figure 1.3. At the end of each, in an environment of ultra-high vacuum, there are meticulously polished and coated mirrors that act as test masses. Once both beams meet back, before the photodetector, they interfere coherently, producing an interference pattern that depends on the relative phase of the two beams. If a gravitational wave crosses the configuration, the distance travelled is perturbed, changing the phase difference of the two beams and, thus, the pattern of interference. This translates into a measurable variation in optical intensity.

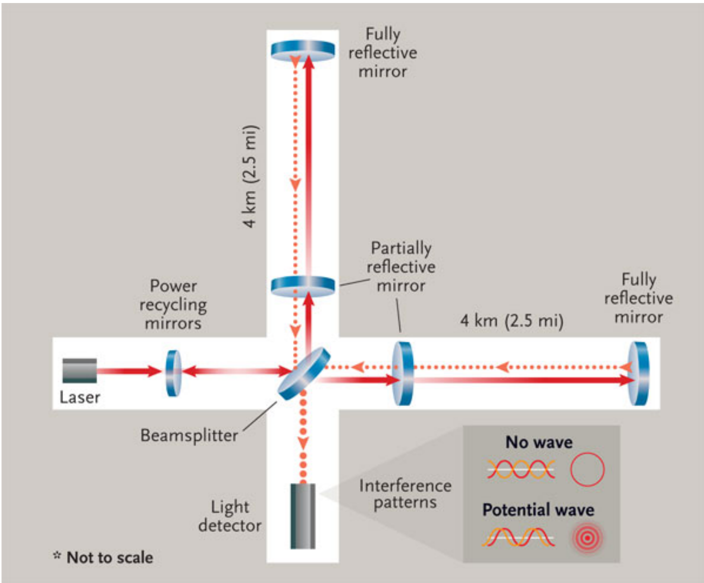

Figure 1.3: LIGO configuration scheme, as an example of gravitational wave detector and Michelson interferometer architecture [1].

As mentioned before, the magnitudes of the perturbations are extraordinarily low, at least 10^{-21} ($[\frac{m}{m}]$). Any disturbance can be noisy enough to bury the signal. There are two fundamental noises setting a limit to the achievable resolution. One of them is Shot Noise coming from the Poisson statistics at which photons arrive to Photodetector, which actually decreases with the power ($\frac{1}{\sqrt{P}}$) relative to the power of the measured signal. The second is Radiation Pressure Noise, which consists on the pressure made by the photons in the surface of the mirror that suffers random momentum kicks too and increases with power ($\sqrt{P}$).

In practice, to achieve the required sensitivity demands sophisticated improvements beyond the architecture of a simple Michelson interferometer. For example, the Michelson's arms are several kilometres long to significantly increase the detector's sensitivity up to levels that allow technology to be accurate, but the system is also required to be highly robust and stable. The platforms which hold the mirrors to redirect light have to remain strongly controlled and isolated to prevent any perturbation from eclipsing the real measurement of interest. There are many details regarding the procedures to isolate a gravitational wave detectors, however, for the sake of clarity and conciseness, just the most relevant to the thesis are explained.

1.2.1 Limitations

To picture the sensitivity of a gravitational wave detector and later noise budgets it is used often used Amplitude Spectral Density (ASD) to frequency graphs. ASD are amplitudes that can cover any range of units (Meters, rads/s, Watts...) over $\sqrt{Hz}$, characterized along a spectrum of frequencies or equivalent units. In the case of the GWD, x axis is unitless as it represents the strain ASD, which can be seen in figure 1.4.

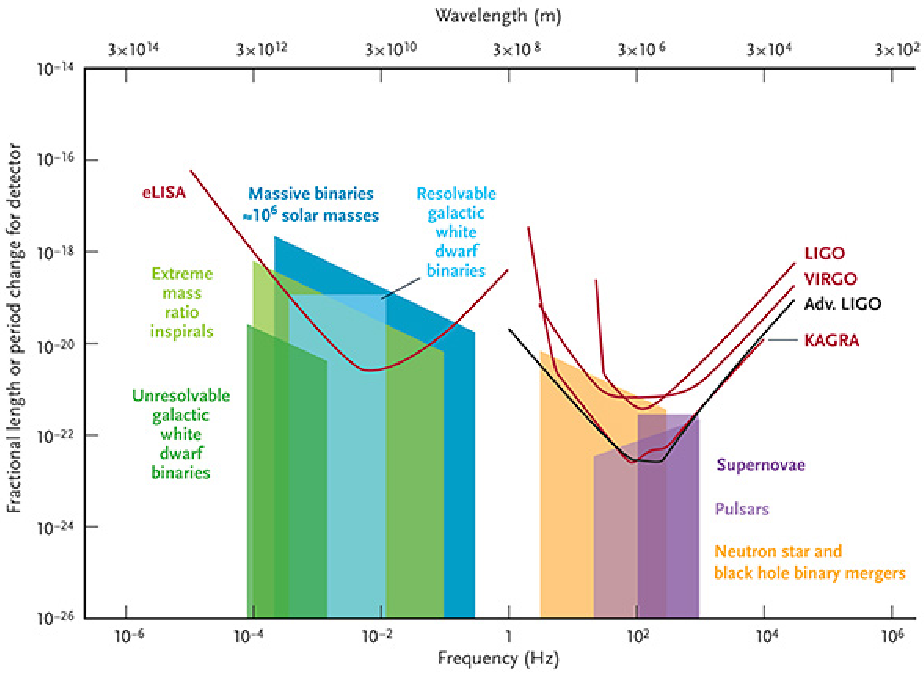

Figure 1.4: Current gravitational wave detector operating bandwidth and their observable events plus the future eLISA observatory [1].

Analysing and addressing the diverse range of noise sources that define the limits shown in Figure 1.4 is one of the greatest challenges in the field, specially at low frequency, becoming the corner stone of the fibre optic gyroscope design. Therefore, the main noises and limitations in the operation of GWDs are outlined next according to the frequency bandwidth.

At the highest frequencies, above a few hundred hertz usually, the noise is dominated by shot noise, as mentioned before, which does not scale with frequency (white noise or f^0). By increasing the power of light or implementing other more sophisticated methods, the resolution in this regime improves.

At the intermediate band, between a few tens of hertz to a few hundred, thermal noise are the dominant contributor. Any mechanical system in thermal equilibrium will exhibit fluctuations driven by temperature and directly related to the dissipation in the system and the quality factor (Q). In summary, there are two thermal noises of particular importance: mirror thermal noise and suspension thermal noise, which arise from the internal thermal excitation of mechanical modes and thermally driven motion of the mirror through the suspension fibres of the mirror. Furthermore, at room temperature, fused silica is becoming the main strategy to mitigate thermal noise problems due to its low mechanical loss (high Q), both, through the mirror and the suspensions manufacturing. However, at cryogenic temperatures, such as the operating environment of the ET, works better silicon following the same reason.

At the lowest frequencies, below 10 Hz, seismic perturbations are the dominant source of noise. They are caused by ocean microseismic activity, human activity, tectonic plates motion and other sources of vibrations from above and below the Earth's surface that are transmitted through the ground. Alike the above mentioned noises, seismic perturbations tend to scale as f^{-2} to f^{-4} below a few hertz, which means that magnitudes build up to huge numbers at lower frequencies. For this case, passive seismic isolation, achieved through multi-stage pendulums, attenuates ground motion above their resonance frequencies. As well, active seismic isolation, consisting on sensor-actuator feedback loops, contributes to suppress motion at low frequencies where the behaviour of the pendulums change. However, further discussions on the later strategy will be presented in the subsequent sections [4].

Furthermore, related to seismic noise but with a different nature is the Newtonian noise. Is the noise describe by gravity gradients caused by fluctuating density distributions in the surrounding medium, mainly originated in the ground or the atmosphere. Since the perturbing medium is gravity itself, no mechanical configuration con mitigate it and it represents a fundamental noise floor below a few ten hertz. It is currently addressed through careful site selection, building underground and the use of seismometers and gravimeter arrays. It represents the challenge for next-generation of gravitational wave detectors [23].

1.3 Einstein Telescope

The current group of gravitational wave detectors; Advanced LIGO, Advanced Virgo and KAGRA (LVK) have already demonstrated how many phenomena can be observed through gravitational waves. However, they are reaching the limits of what they can detect, even though they have been gradually upgraded and from there the previously mentoned titles "Advanced". Therefore, the scientific community demands a new observatory capable of improving current sensitivities by an order of magnitude at least and extending the frequency range significantly further below

10 Hz.

The Einstein Telescope (ET) represents the European proposal for the next generation of ground-based gravitational wave detector, which envelops the European Commission and many research institutions across all the continent. Furthermore, for the first time, it is expected that an GWD surveys the skies continuously for massive events instead of during discrete periods of time, since its proposed architecture implements an additional interferometer which will enable upgrading and maintenance labours to take place without stopping the telescope from operating.

Unlike it's precedents, the Einstein Telescope is proposed to exhibit a triangular geometry rather two perpendicular arms forming an L. Each arm will be 10 km long in an equilateral configuration, providing sensitiveness to both polarisation states of gravitational waves (plus and cross polarization) with just one site. As well, in each vertex there are 2 interferometers, one for low-frequency (LF) detection and another for high-frequency (HF). Due to the difficulty of implementing both systems efficiently in the same interferometer, two different configurations will be built to improve low-frequency and high-frequency performance separately, as showed in figure 1.5. Furthermore, since there are 3 of each kind, redundancy enables effective measuring even during periods of maintenance when one interferometer is under reparation [**?**].

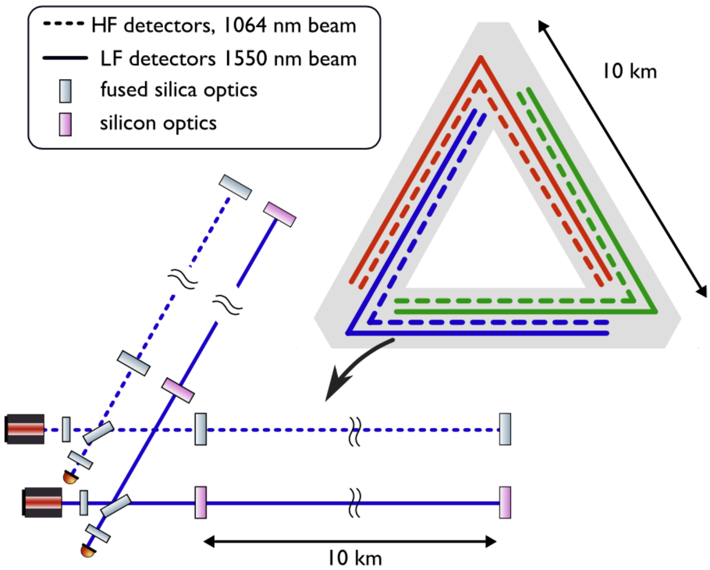

Figure 1.5: Einstein Telescope scheme. Depiction of the three interferometric arms and the two optical approaches (Low-frequency & high-frequency) [3].

Moreover, the increment in length adds more resolution, critical for the LF sensitivity goals and it will located underground, approximately 200-300 metres below the surface. This placement provides a considerable reduction in the noise since ground motion at depth is attenuated, as well as, Newtonian noise because it reduces the surface area exposed to atmospheric and rock density fluctuations. For the moment, three locations are considered, the Euregio Meuse-Rhine region, between Belgium, Netherlands and Germany, the Sardinian region in Italy and the third one in Lusatia, Germany.

The objectives of this scientific observations are wide and addresses questions across astrophysics, cosmology and fundamental physics. Concerning binary systems, the ET will detect binary black holes mergers at rates of hundreds of thousands per year, fostering the investigation of black holes distributions, regarding cosmic history, and black holes themselves. In parallel, binary neutron stars are dimmer but the detection rate is designed to be tens of thousands per year. This high event rate will significantly improve the knowledge on neutron star properties and their equation of state.

In cosmology, the increase in measurable Pulsars, which are constantly pulsing neutron stars that act like clocks of the universe, will allow determining with more precision the Hubble constant H_0. In fundamental physics, the ET enhanced resolution will enable test of General Relativity further beyond.

1.4 Active Isolation

As discussed before, seismic motion represents one of the main limitations in the low frequency range for gravitational wave detectors. Ground motion at a quite site can have an amplitude spectral density of 10^{-7} $m/\sqrt{Hz}$ at 1 Hz, falling as a factor of f^{-2} towards high frequencies [4]. At 10 Hz, the ET is designed to bare noise levels of 10^{-20} $m/\sqrt{Hz}$, so the seismic isolation must provide an attenuation of 10^{13} at least, which becomes more difficult to perform the lower the frequency band.

No passive isolation system has alone provided the required attenuation for this standards to be met at low frequency. The multi-staged pendulum architecture is highly effective above the resonance frequencies of the suspensions, providing the attenuation of f^{-2n}, n being the number of consecutive pendulums. However, below the resonant frequency (usually around 0.5 Hz the dynamics change and the pendulums behave like a rigid body, effectively transmitting ground motion directly to the following stages rather than isolating it [24]. Therefore, to keep ET standards below 1 Hz, it is necessary to implement an active isolation system.

Active (seismic) isolation consists on the use of feedback and feedforward control systems through the measurements provided by the sensors and the active suppression of motion by the actuators, generally, across a targeted frequency bandwidth. This approach requires both, constant sensing of the platform state and constant application of forces to correct the offset of the equilibrium state. Nevertheless, it enables to damp noise below the mechanical resonances of the multi-stage pendulum system and isolate at down to lower frequencies. Furthermore, active isolation facilitates the correction of the offset with respect to the inertial frame due to gradual drifts such as those caused by thermal drifts, oceanic tides or low-frequency disturbances [4].

Concerning the platforms of the gravitational wave detectors, the control approach is that of linear feedback control. In concept, the plant, which is the platform to isolate, is characterized by its transfer function ($P(f)$) that established the relationship between an applied force and a displacement as function of frequency. Then, the sensor measures a variable related to the plant, when is out of the original state it produces an error signal ($e(f)$). To continue, a controller ($C(f)$) processes the error and sends a signal to the actuator, aiming to correct it. The representative equation of a feedback control loop is the following equation, where x_p and x_g are the platform and the ground motion respectively [25].

$$\frac{x_p}{x_g} = \frac{P(f)}{1 + C(f)P(f)} \tag{1.1}$$

The term $L(f) = C(f)P(f)$ corresponds to the open-loop of the system, through it is addressed the stability of the relation ground-platform for the corresponding variable. The bigger $|L(f)|$, the smaller is this relation, which means a more effective decoupling between the ground and the platform, successfully isolating from ground motion. However, the bandwidth over the open-loop term can be big is limited by stability, according to the Nyquist criterion the phase of $|L(f)|$ must stay between 180° and −180° and the phase margin must be at least of 30° for guaranteeing a robust stability. Considering phase lag introduced by the sensors, the actuators and the computational processing, to keep an effective isolation over large bandwidths is a challenge.

In practice, two strategies are employed at the same time. Inertial sensors like geophones or seismometers, measure the absolute motion with respect to the inertial frame of the platform. However, these sensors exhibit a noise floor which scales as (f^{-2}) or worse, considerably limiting their performance below 0.1 typically. On the other side there are relative displacement sensors like capacitive sensors or optical levers, which measure the displacement relative to another structure of reference, enabling to maintain a defined position over time by gradual drifts. In the end, both sensors are combined to achieve the best performance, benefitting from the better performance of relative sensors at low frequency and the superior mid frequency performance of inertial sensors.

On the other side, feedforward control provides an additional source of noise compensation, specially for disturbances that can be measured independently, like a seismic wave passing through another platform. If a sensor is capable of measuring a disturbance before it reaches the main platform, it can send a signal to the actuators to compensate for the wave, without concerning about the stability problems of closed loops.

1.4.1 Inertial Horizontal Sensor

An inertial sensor is an instrument which measures motion through the relative displacement between a proof mass and the sensor frame. This displacement can be sensed using various readout techniques, such as capacitive, inductive, or interferometric measurements. Regarding seismic isolation for gravitational wave detectors, these sensors are the highest performing at mid to high frequencies, reaching orders of 10^{-9} $m/s^2/\sqrt{Hz}$ in acceleration [26]. At low frequencies, sensors' noise floor limit the detector's capacity to measure gravitational waves.

The most common sensors inside this category are based on the mass-spring principle, where a proof mass rests inside a case for isolation and is hold by a restoring element like a physical spring or an electric field. Then, the displacement with respect to the case is effectively measured above the resonance frequency of the instrument with a transducer. However, below the resonance frequency, the mass tends to with the case, becoming insensitive to external motion, whereas above and the higher the frequency goes, the proof mass rests more unperturbed through it's relatively high inertia, acting as an internal inertial reference frame while the case moves with the platform. This frequency-dependent behaviour is a shared characteristic among all inertial sensors, no matter the configuration or the structure.

Depending on the architecture and the restoring force acting on the mass, inertial sensors can be separated into different categories. The first one is represented by the classical mass-spring sensors, which are the geophones, seismometers and accelerometers where the spring is often a physical coil or lead spring. The second category consists of balanced sensors, where a high-inertia proof mass is suspended by a thin, low-stiffness flexure precisely at its centre of mass and, unlike classical mass-spring sensors, the dominant restoring torque comes from gravity rather than a mechanical spring. These are relatively new in the state of the art of sensors, introduced for improving performances in tilt measuring at low frequencies and mainly represented by beam balance sensors. The third family, and the newest one, are the superconducting accelerometers, in which the proof mass is levitated through electromagnetism in a superconducting cavity.

The inertial horizontal sensor follows a mass-spring architecture, being the most widespread in seismic isolation. It consist on a mass, a restoring force that guides the later and an enclosure which moves with the platform. When the platform is subject to a perturbing motion, the case, or enclosure, follows rigidly the movement but the proof mass remains relatively in the same position due to its inertia. The relative motion between the mass and the case is proportional to ground displacement when the frequency is above the resonance frequency $f_0 = \frac{1}{2\pi}\sqrt{\frac{k}{m}}$, where k is the corresponding stiffness of the spring and m is the proof mass. However, below f_0 the mass moves with the case so the relative displacement ends up dropping as f^2. Therefore, looking at the formula, reducing the spring stiffness or increasing the proof mass lowers the resonance frequency, spanning for a bigger operational bandwidth.

Geophones are very simple sensors and consist on a electric-conductive coil settled around a magnet which produces a voltage when forced to move from the equilibrium position. The output is proportional to the velocity amplitude of the ground motion above resonance, usually around a few Hz, and they are cheap and robust. Unfortunately, their relatively high resonance frequency stands as their main limitation, poorly performing at sub-Hz frequencies, mainly due to the compromise of reliability and having a very heavy or soft system [26].

On the other side, broadband seismometers provide a higher performance. Through anti-spring configurations or close loop desing, they can achieve resonance frequencies down to 0.01 Hz. For example, the STS-2 is used too in gravitational wave detectors infrastructure, achieving self noise levels close to the New Low Noise Model (NLNM) seen in graph 1.6. The later represents Earth's seismic noise at low frequencies, between 0.001 and 50 Hz and is the main seismic profile in quite locations in absence of anthropological noise. Sensors of this performing level are used as the main low-frequency sensors in the Advanced LIGO for several platforms, usually blended with geophones to obtain a far bigger operating bandwidth.

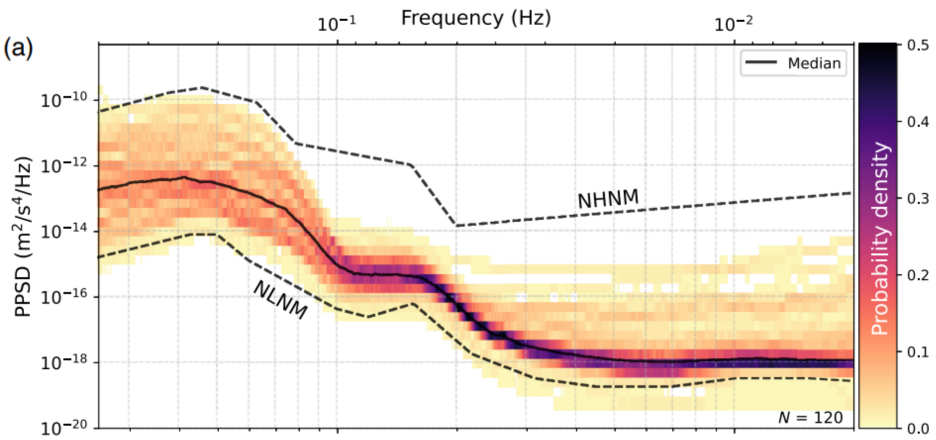

Figure 1.6: Probability PSD Noise model for Earth's seismic perturbations in translational acceleration units $[(m/s^2)^2$ [4].

In the end, the Brownian noise sets one of the biggest challenge when improving mass-spring sensors. The energy dissipation through motion of the suspension and the subsequent thermal fluctuations are the cause of this limit. Therefore, the resolution can be improved by increasing the quality factor, which is pursued by in next-generation seismometers through the implementation of materials such as fused silica with low mechanical loss.

1.4.2 Tilt-Horizontal Coupling

A fundamental limitation of inertial sensors in the context of active seismic isolation is the tilt-horizontal coupling. Any inertial horizontal accelerometer, no matter its quality or configuration, is physically unable to distinguish between a true translational acceleration $\ddot{x}$ and the relatively slow tilt θ of the platform. The reason is purely geometrical. When a platform tilts by a small angle θ, gravity projects onto the horizontal axis of the accelerometer with a magnitude $g\theta$, producing an output identical to the one produced by a real horizontal acceleration, as depicted in figure 1.7. The measured signal is therefore always the sum of both contributions, $a_{meas} = \ddot{x} + g\theta$, and no amount of signal processing can separate them from a single accelerometer measurement alone [11].

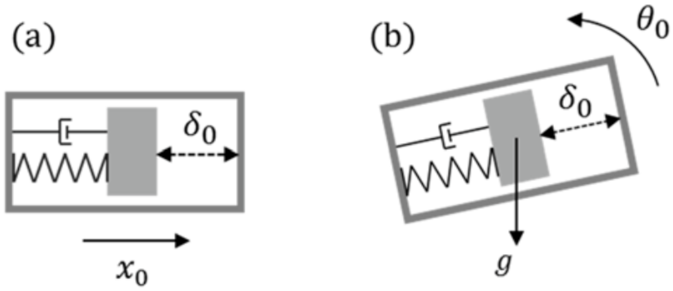

Figure 1.7: Tilt-horizontal coupling scheme through an horizontal inertial sensor [5].

This coupling is described by the following transfer function, which relates the measured horizontal displacement δ with the tilt θ induced by the platform [27]:

$$\frac{\delta}{\theta} = \frac{g}{s^2 + 2\mu\omega_s s + \omega_s^2} \tag{1.2}$$

where g is the gravitational acceleration, ω_s is the resonance frequency of the sensor and μ is its damping ratio. As observed in Figure 1.8, the transfer function behaves as a second order low-pass filter. Above the resonance frequency ω_s, the sensor's inertia decouples it from the platform horizontal motion and the sensitivity to tilt rolls off as $1/f^2$, quickly becoming negligible. However, below ω_s, the transfer function approaches g/ω_s^2, meaning the tilt contribution is transmitted completely into the acceleration measurement. Since seismic inertial sensors typically have resonance frequencies in the range of 0.1 to 1 Hz, this problematic regime coincides precisely with the low-frequency band where the ET demands the highest active isolation performance.

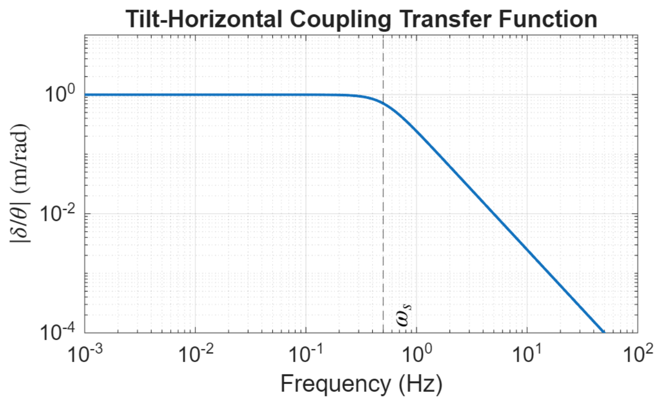

Figure 1.8: Tilt-horizontal coupling transfer function. ω_s denotes the natural frequency.

The transfer function between the sensed and the true horizontal translation of the platform is given by Equation 1.3 [27].

$$\frac{\delta}{x} = \frac{\omega^2}{s^2 + 2\mu\omega_s s + \omega_s^2} \tag{1.3}$$

Below the resonance frequency, this transfer function rolls off as ω^2/ω_s^2, meaning the sensor becomes increasingly insensitive to true translational motion at low frequencies, as shown in Figure 1.9.

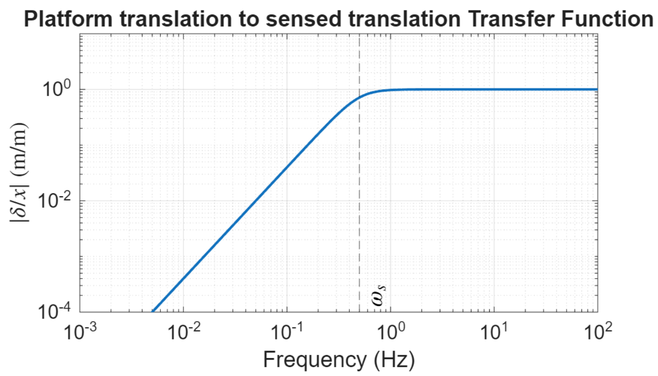

Figure 1.9: Sensed translation to true platform translation transfer function.

Comparing both figures, it is apparent that the sensitivity to tilt and the sensitivity to translation both degrade towards low frequencies. To quantify this directly, Equation 1.4 expresses their ratio:

$$\frac{\delta_x}{\delta_\theta} = \frac{\omega^2}{g} \tag{1.4}$$

As represented in Figure 1.10. This ratio falls steeply as ω^2, independently of the resonance frequency, mechanical loss, or any other sensor parameter. It constitutes a fundamental result: regardless of the quality or configuration of the inertial sensor, its ability to distinguish true horizontal translation from tilt degrades irreversibly towards low frequencies, establishing the need for a dedicated rotation sensor in the bandwidth of interest.

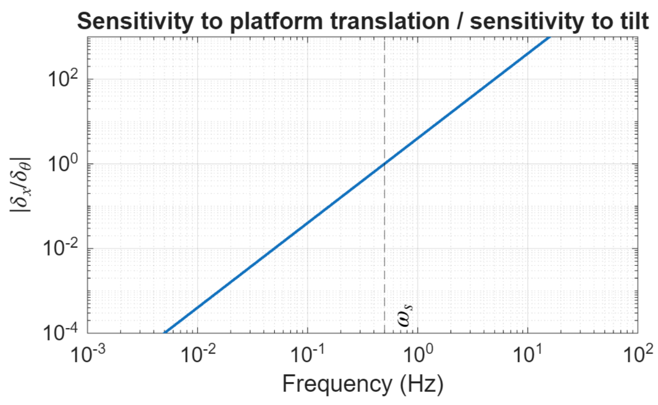

Figure 1.10: Ratio between the sensitivity to translation and the sensitivity to tilt.

The practical consequences for active isolation are significant. At low frequencies, the feedback controller receives a horizontal acceleration signal dominated by ground tilt rather than true translational motion, driving the actuators to correct for a displacement that does not exist and injecting noise into the platform instead of suppressing it. Furthermore, since seismic tilt scales steeply towards low frequencies, the gravity coupling term grows rapidly compared to the translation sensitivity below 1 Hz, quickly overwhelming the true translational signal and rendering horizontal inertial sensors unreliable in this band.

On the other hand, some approaches include sets of several vertical sensors to differentiate vertical motion from tilt and, consequently, separate it from horizontal measurements. However, this strategy requires a sufficiently large sensor separation to resolve the tilt angle from the differential vertical signal, which becomes increasingly difficult to achieve towards lower frequencies where, consequently, wavelengths tend to be larger. Eventually, it grows bigger than the actual platform dimensions, making their implementation more difficult maintaining appropriate levels of sensitivity. Therefore, an independent measurement of θ is necessary to subtract the tilt contribution from the accelerometer output and recover the true translational signal. This is the main motivation for the development of a dedicated high-sensitivity rotation sensor, and decoupling tilt from translation represents a fundamental requirement for achieving the ET isolation targets below 1 Hz

Objective

The main ojective of this thesis is to investigate the possibility to design a rotation sensor to enhance seismic isolation at low frequency. To this end, a gyroscope model is developed. Its sensitivity and noise sources are investigated and evaluated in relation to several key parameters. Conlusion are then drawn from the results of this study. In addition, this work aims to evaluate the methodology and design choices made throughout the project, providing future feedback for other engineers and scientists, besides an introspective judgement of my own job.

The procedure followed in the body of the thesis starts with the display of the different tilt-sensor technologies through thoughtful investigation. Afterwards, the later are discussed to properly make a choice and then, the different steps of the design process are stated, providing justification to the details of the architecture.

The targeted rotational sensing resolution is approximately 1–10 nrad/s/sqrt(Hz). This requirement was derived from active isolation simulations of a simplified platform model. Such performance would enable up to two orders of magnitude of isolation from seismic motion down to 10 mHz.

Chapter 2

State of the art

Achieving the rotational sensitivity required for the Einstein Telescope isolation platforms demands understanding and improving the capabilities of conventional instrumentation. A broad range of sensing technologies have been developed over the decades to measure ground tilt and rotation, each based in distinct physical principles and targetting different purposes, from navigation and orientation to seismology and gravitational wave detection. Therefore, this section presents an overview of the tilt-measurement techniques available to date, their operating principles, their applications, and their performances, stating the base ground for this project.

2.1 Gyroscopes

A gyroscope is an instrument that measures angular displacement or velocity with respect to an inertial reference frame, with no need of any external reference.

The physical principles behind gyroscopes can be separated into 2 categories. First, there is the conservation of angular momentum, which prevents spinning masses to change the orientation of its rotation axis and offsets around it can be translated into measurable signals. Second, there is the Sagnac effect, which arises from the coherent interference of two waves after they travel in different directions or through a perimeter in opposite senses of circulation, producing a non-reciprocal phase shift when rotation takes place in the same plane.

For gyroscopes in controlled systems, the most representative figures are the angle random walk (ARW), which corresponds to the integrated angular noise, normally in $\mu rad/\sqrt{Hz}$ or $nrad/\sqrt{Hz}$, together with the bias instability that states the long term drift of the measure when there is no rotation. However, for the applications targeted by this thesis with sensitivities at the level of $nrad/\sqrt{Hz}$ and below, between 10 mHz - 1 Hz, only the highest performances can be competent.

2.1.1 Mechanical and MEMS Gyroscopes

Spinning rotors were the earliest gyroscopes, using the rigidity of angular momentum to determinate rotation. These mechanical instruments presented a classical gyroscope with a spinning mass. It consists on a rotor mounted in a gimbal that allows the main body to remain fixed while the surrounding rings or structural features rotate freely around it. The rotation is measured by the misalignment of the free-rotating structure and the spin axis. Mechanical gyroscopes have improved greatly, enough to settle a reliable instrument in orientation determinations for the aerospace industry in the 20th century, however, issues like their reliance on bearings or tendency to wear toss them aside in modern [26].

On the other side, Microelectromechanical Systems (MEMS) dates from the 1980s and have competently evolved into millimetric devices used all around the world nowadays. MEMS gyroscopes operate based on the Coriolis effect, where a proof mass that is oscillating in one axis experiences rotation, the Coriolis effect makes it rotate too in the orthogonal axis proportionally to the external angular rate. Currently, MEMS are now small, light and cheap, with fairly good performance, so they are the favourite choice for many products, such are phones, cars, UAVs... However, their noise values are around 10^{-4} $rad/\sqrt{Hz}$ mainly due to thermal and mechanical noise. Furthermore, their small proof mass leads to a relatively high resonance frequency, making them unsuitable for low-frequency sensing application, like GWD seismic isolation [28].

On top of that, there are Hemispherical Resonator Gyroscopes (HRG), which make use of the rotation of the vibration pattern of a thin hemispherical shell. Their performance is relatively better than MEMS, coming to 10^{-6} $rad/\sqrt{Hz}$, having no moving or rubbing parts and implemented in space navigation, but still far from ET requirements.

As well, there are other gyroscopes used in the modern industry such as the Dynamically Tuned Gyroscopes (DTG) which also uses a gimbal and is used in the space sector. There are the Quartz Rate sensors or Quartz MEMS too, which are vibrating gyros that use piezoelectric quartz instruments and perform considerably better than MEMS but do not perform well enough for gravitational wave detection.

Beam Balance Gyroscope

The beam balance is one of the options with highest potential for the low frequency environment. It consists on a proof mass with high inertia supported only at the centre of mass by a non-restrictive rotation joint. Usually, the mass is suspended by very low stiffness flexures and the mass is tuned to lay at these flexures, so when the platform tilts, the proof mass stays in the same position, gradually recovering the orientation with respect to the platform through the torque applied by the flexures. The starting relative rotation of platform w.r.t. the proof mass, usually a longitudinal or circular beam, constitutes the signal, as depicted in figure 2.1 [6].

The dynamics of the beam balance and the relevant transfer functions are described in the

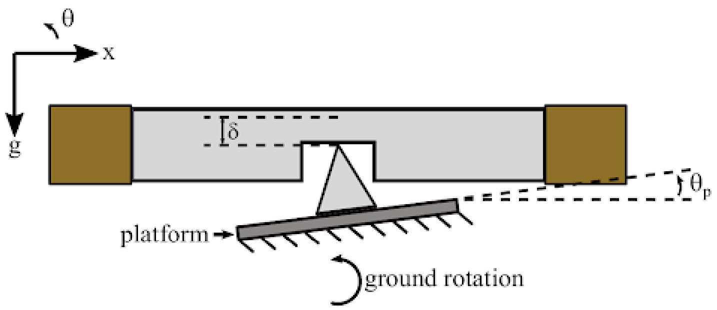

Figure 2.1: Transfer Function representing beam balance sensitivity to rotation [6].

next equation, where it relates the beam tilt θ with the platform tilt θ_p and the horizontal ground acceleration a_x [6].

$$I\ddot{\theta} + k_a(1 + i\phi)(\theta - \theta_p) = \tau_{ext} - Mg\theta\delta - M\ddot{x}_p\delta \tag{2.1}$$

where I is the moment of inertia, k_a the stiffness to torsion, ϕ the loss factor, M is the proof mass and δ the offset between the Centre of Mass (CoM) and the pivot point. On the other side, the horizontal acceleration $\ddot{x}_p$ represents the tilt-horizontal coupling as the term is. It constitutes one of the main design challenge for achieving reliable rotation sensing at low frequency. Introducing the previous equation in the dynamics of the beam balance, the resulting transfer function between sensed and platform tilt is [6]:

$$\frac{\theta_a}{\theta_p} = \frac{\omega^2 - \omega_g^2}{\omega^2 - \omega_0^2(1 + i\phi)} \tag{2.2}$$

where w_0 is the resonance frequency of the beam and w_g is a characteristic frequency related to the CoM misalignment term which is $w_g = \sqrt{Mgd/I}$. As the other inertial sensors, the beam balance performs effectively above the resonance frequency, measuring the ground tilt as relation of $T.F. \approx \omega^2/\omega^2 = 1$. On the other side, below the resonance the sensor acts like a pendulum, losing sensitivity as $T.F. \approx \omega^2/\omega_0^2$, until the balance between the gravity term and the resonance frequency is reached $T.F. \approx \omega_g^2/\omega_0^2$, as observed in graph 2.2. Also, it can be observed a zero below the resonance frequency corresponding to the "gravity frequency", which is the one represented by w_g, where the numerator comes to 0. However, looking back again at the gravitational frequency expression $w_g^2 = Mgd/I$, the zero is only given when the pivot angle is above the CoM, since the misalignment d turns negative otherwise and the numerator cannot become 0 or negative by any other means, as seen in graph 2.2. At it, the gravitational restoring torque cancels with the inertial torque induced by the ground motion, making the sensor move in perfect synchrony with the platform.

Parallelly, the main concern on the design of a beam balance gyroscope is the misalignment with the CoM, whose direct and main consequence is the sensitivity to translation. The transfer

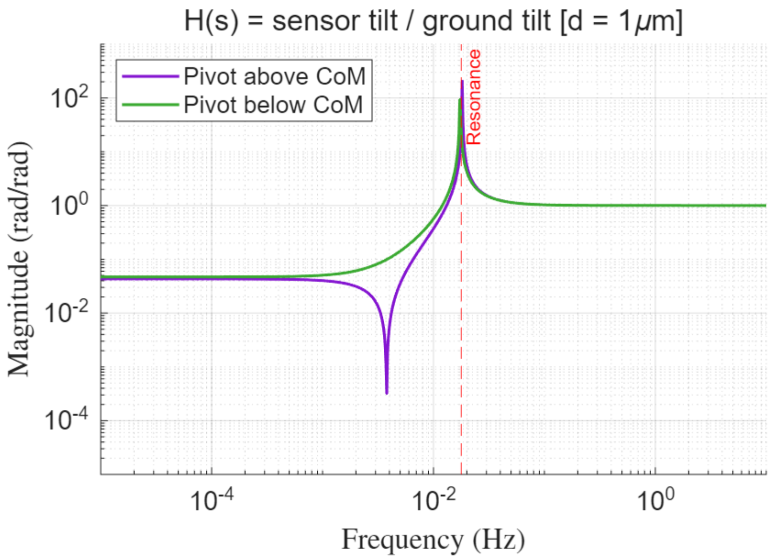

Figure 2.2: Transfer Function representing beam balance sensitivity to rotation.

function between sensed tilt and horizontal translation is given in graph 2.3. It shows that horizontal motion of the platform on which the sensor is mounted contaminates the rotation measurement. This effect becomes particularly problematic when the sensor's sensitivity to translation approaches its sensitivity to rotation. As shown in Equation 2.1.1, the sensitivity to translation is proportional to d. Therefore, a very careful tuning of the CoM position is needed to minimize it [6].

$$\frac{\theta_a}{\ddot{x}} = \frac{-Md}{I(\omega_0^2(1+i\phi)-\omega^2)} \tag{2.3}$$

Bringing down the misalignment is the main research area of these sensors, which generally count with tens of μm, but various techniques have been already developed to achieve tens of nm, including iterative grams adjustments in the mass and remote tuning mechanisms for sensors in the vacuum chamber.

Regarding the tilt-to-signal measuring process, three approaches have been the more habitual employed to translate the tilt of the beam into an electrical signal. Sensing with capacitors is one and is easy to implement but present significant non-linearities and spontaneous electrical noise problems at low frequencies. As well, inductive sensors were employed too, using LVDTs, but they are susceptible to thermal drift and is an increasing problem towards low frequencies. Finally, optical techniques are the currently best-performing choice. Walk-off sensors (WOS) and Michelson interferometers located at both extremes of the beam, reaching noises below $nrad/\sqrt{Hz}$ orders at the readout, without additional mechanical losses.

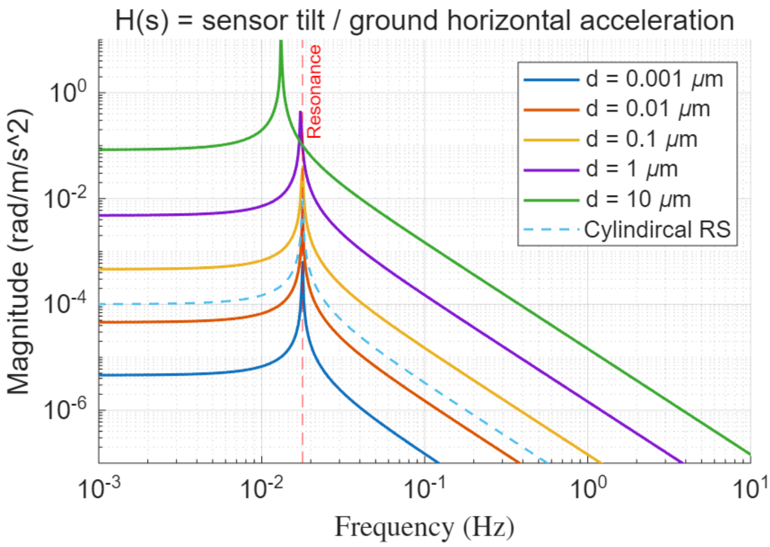

Figure 2.3: Transfer Function representing sensitivity to ground horizontal accel. depending on the misalignment d. Considers also the least d achieved in the state of the art (Cylindrical RS).

ALFRA Balance Beam

The ALFRA sensor was reported in 2021. It developed a resonance frequency of 50 mHz and a misalignment of 5 μm, working efficiently down to 2-3 Hz, since it was targetted to work in the concerning frequency regions of the Virgo and the Einstein Telescope, whose observation band extends down to 2 Hz. Its is the most representative for the family of the beam balance detectors. As observed in figure 2.4 it is constituted by a long and high-inertia proof mass with the shape of a beam, supported in the midpoint as close as possible of the CoM, with light interferometric readout to measure the proos mass's rotation with high resolution (WOS readout). It can be highlighted that ALFRA demonstrate competitive performances in this band, but the resolution at lower frequencies is insufficient for the ET design requirements [6].

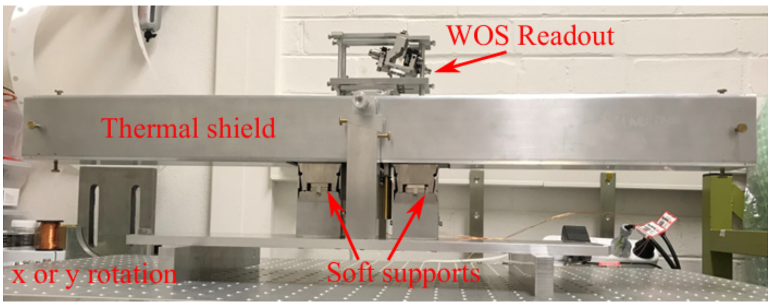

Figure 2.4: ALFRA beam balance. Horizontal Perspective [6].

Naples University Beam Balance

This beam balance is being developed at the University of Naples by E. Calloni and collaborators of the Archimedes project and the Virgo observatory. They mainly target seismological isolation for next-generation gravitational wave detectors such as Virgo and the Einstein Telescope. In 2021 they demonstrated sensitivity levels of $8 \cdot 10^{-11}$ $rad/\sqrt{Hz}$ at a few Hz, with a constant resolution of a few 100 $prad/\sqrt{Hz}$ above 10 Hz and a CoM tuned to be within 10 μm of the centre of rotation. However, as well as the previous design, the choice of a light arm favours the sensitivity for measuring the torque, but it limits the instrument's performance for tilt at lower frequencies. This is because a lighter arm reduces the moment of inertia, raising the resonance frequency and limiting the sensitive bandwidth at low frequencies [29].

In 2024 several improvements to the design were reported, including an increase in the beam length to 0.5 m. Operating in a quiet environment, they achieved a torque sensitivity of $\tau_n \approx 2 \cdot 10^{-12}$ $Nm/\sqrt{Hz}$ at 10 mHz with a minimum of $7 \cdot 10^{-13}$ $Nm/\sqrt{Hz}$ around 40 mHz. This design represents one of the most sensitive room-temperature beam-balance implementations to date.

Quartz Rotation Sensor

The Quartz Rotation Sensor (QRS) has been developed by Venkateswara and collaborators in 2021 and introduces subtly different approach [30].This instrument uses a quartz resonator as the spring element instead of a passive torsional flexure, so when the platform is disturbed, the corresponding torque shifts the resonator's frequency proportional to the applied rotation. For using a resonator, it reaches surprisingly low noise levels and an excellent stability. The QRS has achieved a noise floor of approximately 45 $prad/\sqrt{Hz}$ around 1 Hz, a readout sensitivity of 0.1 $nrad/\sqrt{Hz}$ above 50 mHz and $2 - 3$ $nrad/\sqrt{Hz}$ above 20 mHz with a resonance frequency of 0.1 Hz and a CoM misalignment of 13 μm. Furthermore, the reason the noise floor is so competitive even below the resonance frequency is through the implementation of an electromagnetic anti-spring, extending the operating bandwidth.

Cylindrical Inertial Rotation Sensor

The cylindrical rotation sensor is a gyroscope developed with the efforts of several universities but mainly represented by the Washington University [7]. This particular gyroscope has a cylindrical proof mass with two interferometers pointing at both extremes of the cylinder, where two plates stand out of the proof mass, as observed in figure 2.5a. In 2023, the centre of mass is tuned to be < 22 nm corresponding to a transactional sensitivity of < 1.3 $\mu rad/m$, as well as achieving a flexure thickness of 14 μm, with aluminium materials to maximize thermal uniformity and with remote tunable masses to adjust the CoM inside the vacuum chamber. With this characteristics it reaches a noise floor of 1 $nrad/\sqrt{Hz}$ above 30 mHz, of 0.2 $nrad/\sqrt{Hz}$ above 100 mHz and

5 $prad/\sqrt{Hz}$ at 1.5 Hz, as represented figure 2.5b, with a resonance frequency of 17 mHz. These are really competitive performances for the Einstein Telescope requirements, ensuring effective isolation at 1 Hz, and improving the performing bandwidth below it compared to other gravitational wave detectors.

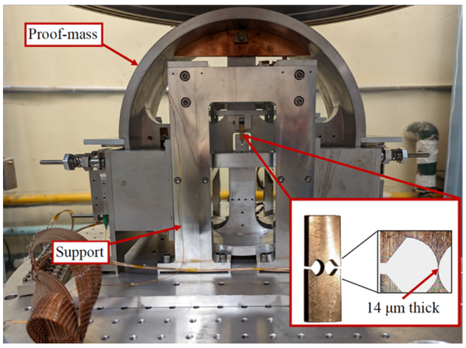

(a) Cylindrical Rotation Sensor horizontal view with the depiction of the restoring mechanism (the flexure).

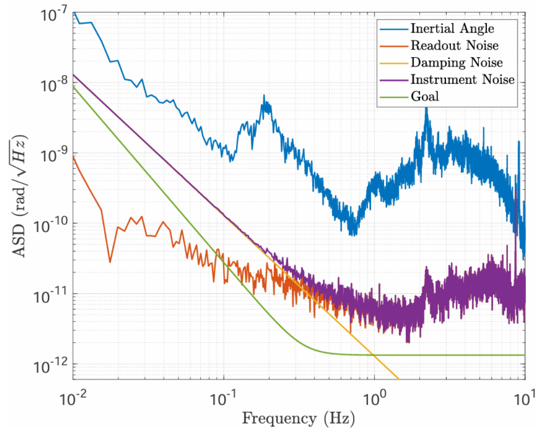

(b) CRS Noise floor and its components, provided by the CRS collaborators.

Figure 2.5: CRS architecture and resolution [7].

2.1.2 Optical Rotation Sensors

The principle on which optical rotation sensors are based is the Sagnac effect, demonstrated the first time experimentally by Georges Sagnac in 1913. When two beams circulate around an optical perimeter in opposite directions they accumulate a phase shift $\Delta\phi$ depending on the angular rate Ω of rotation, as visually represented in figure 2.6:

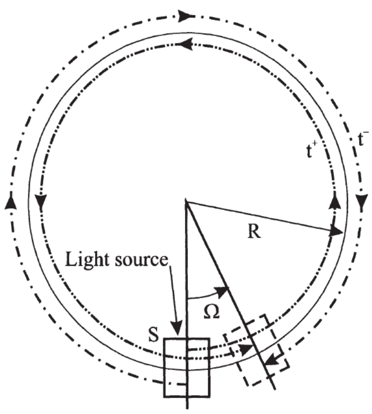

Figure 2.6: Visual description of the Sagnac effect for circular perimeters (FOGs) [8].

The Sagnac effect is mathematically described by the following equation as well [31] [11]:

$$\Delta\phi = \frac{8\pi NA}{\lambda c}\Omega \tag{2.4}$$

where A is the area enclosed by the perimeter, N is the number of turns around the enclosed area, λ is the wavelength of the optical source and c is the speed of light in vacuum. It must be highlighted that this effect is independent of the position of the rotation axis, the refractive index of the optical path and any translational motion of the enclosed area. Therefore, an optical sensor supported on the Sagnac effect is completely insensitive to translational motion, at least a priori. On the other hand, inertial sensors mentioned before, rely on a proof mass that inevitably relates translation and rotation. This makes the Sagnac effect very suitable for seismic isolation.

Taking a look at the previous equation, it does not follow the habitual rules of mechanical systems, it does not include frequency nor time based relations. It is a flat transfer function from DC to the infinite. It has no natural frequency or roll-off frequency. On the other side, mechanical sensors, as mentioned before, present a roll-off falling as f^2 below their resonance frequency and, particularly, beam balance require a very fine tuning of the CoM to remain competitive.

Ring Laser Gyroscopes

The Ring Laser Gyroscopes (RLG) was the first implementation of the Sagnac effect. In this device, two laser beams from the same optical source propagate in opposite directions through a monolithic optical cavity, being generally a gas like helium-neon, and the measurable variable manifests as a frequency split between the two beams, also called beat frequency [32] [11].

$$\Delta f = \frac{4A}{\lambda P}\Omega \tag{2.5}$$

where A is the area again, P is the perimeter and Δf is the measured difference in frequency. As it can be noticed, this signal is linear and not dependent on the frequency. It could be adapted to display the tilt or the angular acceleration rather than angular speed. These equations would present a frequency dependency but would not feature any resonances, zeros or roll-off.

Since the sensitivity is proportional to the enclosed area, RLGs encourage to build big devices for precision applications, for example, the Gross Ring G at the Wettzell Geodetic Observatory in Germany, the second largest one ever built, after the ROMY from the LMU in Germany too. It has an area of 16 m^2, achieving a rotation sensitivity of almost 10^{-11} $rad/(s\sqrt{Hz})$, which measures the Earth's rotation rate and detects polar motion [26]. Furthermore, the Virgo collaboration has developed an RLG with a diameter of 1.82 m, achieving a sensitivity of 10 $nrad/\sqrt{Hz}$ below 1 Hz [26].

On the other side, in the real implementation in gravitational wave detectors, there manifests several constraints. The construction of the monolithic cavity makes the RLGs bulky and rigid, so inside that large area, the instrument cannot be folded or adapted to fit in the platform structure easily. In addition, they are specially delicate structures which require high calibrations and strictly-controlled environments to operate. However, RLGs suffer from a nonlinear effect at low rotation rates which causes the measured signal to vanish, creating a band around 0 rotation where no beat frequency is obtained. It is the lock-in that happens when backscattered waves from both beams interact at the photodiode, and it can only be surpassed by dithering the cavity. This technique introduces considerable vibrational noise that is not welcome in isolation platforms for high-precision measurements.

Fibre Optic Gyroscopes

The Interferometric Fibre-Optic Gyroscope (IFOG), more commonly referred to simply as a fibre-optic gyroscope (FOG), operates similarly to RLG. Instead of a laser cavity, the two counter-propagating beams travel through a coil of optical fibre as depicted in figure 2.7. The Sagnac effect is here represented by a phase shift $\Delta\phi$ [31] [11].

$$\Delta\phi = \frac{2\pi LD}{\lambda c}\Omega \tag{2.6}$$

where L is the total fibre coil length, D is the coil diameter, λ, c and Ω are, as mentioned before, the wavelength of the optical source, the speed of light in vacuum and the angular speed of the real rotation, respectively. As it happened with the RLG, the area enclosed is proportional to the sensitivity, but also the times that area is surrounded by the fibre, meaning, not only the area but the length of the trip increase sensitivity. In absence of a rigid cavity, the FOG fibre coil is flexible and adaptable to a wide variety of factors, which makes it notoriously easier to test and install, and it is perfectly operational with a commercial optical source whilst RLG requires a specifically designed lasing cavity.

To properly assess FOG's performance, the figures of merit are characterised next. The Angle Random Walk (ARW), represents the white noise floor of the rotation output, expressed in $rad/(s\sqrt{Hz})$. The Bias Instability, represents the stability limit to low frequencies. Is the point where noise stops being averaged down, no longer improving the measurement. The scale factor K, converts the detector output into rotation rate and its linearity and thermal stability directly affect the accuracy of the instrument. There are also other characteristics such as Shot Noise and Relative Intensity Noise (RIN), which characterize the quality and resolution of the FOG, but they will be addressed in the main body of the thesis as they constitute a driving factor for architectural decisions.

Regarding the state of the art of commercial FOGs, it can be represented by two instruments at the peak of performance levels. The EXAIL Astrix 200 achieves an ARW of $2.9 \cdot 10^{-8}$ $rad/(s\sqrt{Hz})$ and a bias instability of $2.4 \cdot 10^{-9}$ rad/s over integration times of the

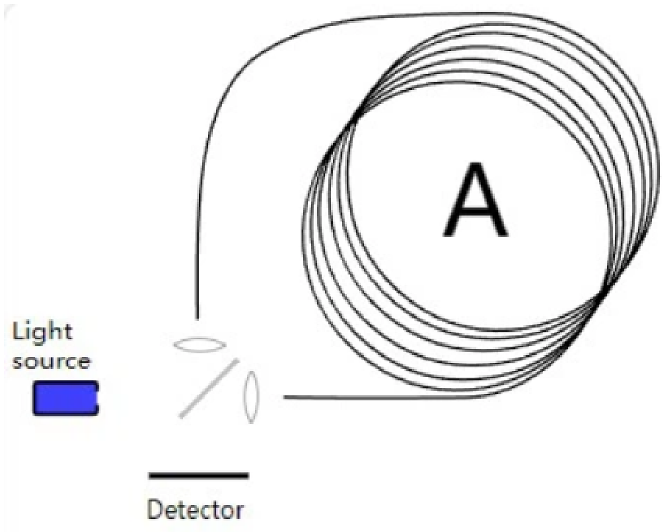

Figure 2.7: FOG working principle. Splitter + Fibre Coil [9].

order of 1 000 seconds, with a scale factor linearity of 10 ppm [33]. Originally designed for spacecraft attitude control, it represents one of the most reliable and mature commercial FOGs available, centred in space navigation applications. As well, it is worth mentioning that it consumes 22.5 W, which introduces a heat load not negligible for a vibration and thermally sensitive environment, such the ET isolation platform. On the other side, the BlueSeis3A, from the same company, is the highest resolution FOG available in the market to the best of my knowledge. It has a self noise floor of $2 \cdot 10^{-8}\ rad/(s\sqrt{Hz})$ between 0.01 and 100 Hz. Nevertheless, both instruments do not reach the noise floor required to meet ET isolating expectations, and they are also limited by their initial commercial size design. Since sensitivity scales directly with the enclosed area, these models cannot achieve their maximum performance, whereas a custom large coil designed to bring resolution to the lowest value possible could overcome this performance gap. This is the main motivation for the work presented in the following chapters.

Chapter 3

Fibre Optics Gyroscope Design Evolution

In this section, the body of the thesis is going to be represented through different steps, following the most intuitive process for the sake of the best understanding. Starting from the most basic and functional architecture, all the components and characteristics are covered, implementing the subsequent improvements until the final configuration is achieved.

3.1 Gyroscope Choice Comparison

The next subsections are going to compare the different potential choices and competitive approaches that could have been taken. These are, the Beam Balance Gyroscope, the Ring Laser Gyroscope and the dichotomy whether to buy the BlueSeis3A or customizing the design to build the FOG from scratch.

3.1.1 FOG vs. Beam Balance

In the past section, both technologies have been reviewed in the context of the ET isolation platform and both have demonstrated a resolution in orders of tens of $nrad/\sqrt{Hz}$ in highly controlled environments and conditions. Therefore, both technologies are going to be assessed more profoundly to determine which is more suitable for the ET requirements.

The main difference between both are the sensing principles, which follow distinct transfer functions. On one side, the beam balance is a mechanical instrument whose sensitivity to rotation comes from the high inertia of the proof mass and the strong alignment between the CoM and the pivotal point, restoring its original position by the subtle torque of a very thin torsional flexure. Above its resonance frequency (ω_0), the beam balance behaves as a reliable sensor and measures ground rotation effectively, whereas below, the sensitivity drops as factor of f^2 falling towards zero at DC. The best performing sensor of this kind is the Circular Inertial Rotation Sensor from the Washington University, which stands with a natural frequency of $\omega_0 = 2\pi \cdot 17$ mHz ≈ 100 mrad/s It is already close to the lower bound of the active isolation bandwidth we are targetting ($[10\ mHz - 10\ Hz]$) to achieve ET isolation requirements [7].

On the other side, the FOG presents a transfer function flat from DC up to the readable bandwidth, since the physical phenomena in which it relies (the Sagnac effect) is completely independent of the frequency, without resonance or roll-off frequency. This behaviour is represented by the Sagnac equation, which also states the transfer function between the two light beams relative phase shift $\Delta\phi$ and the sensor's angular speed Ω [31]:

$$\Delta\phi_s = \frac{2\pi LD}{\lambda c}\Omega \tag{3.1}$$

where the Sagnac coefficient is $K_S = \frac{2\pi LD}{\lambda c}$. As shown in Figure 3.1, the FOG maintains the sensitivity across the bandwidth of interest and while inertial sensors start degrading below their resonance. This argument already sets a genuine and practical interest in FOGs above, even, the best beam balance gyroscope. In addition, the flat transfer function of the sensor usually renders controller design easier by improving closed loop stability and avoiding dynamic coupling with the platform on which it is placed.

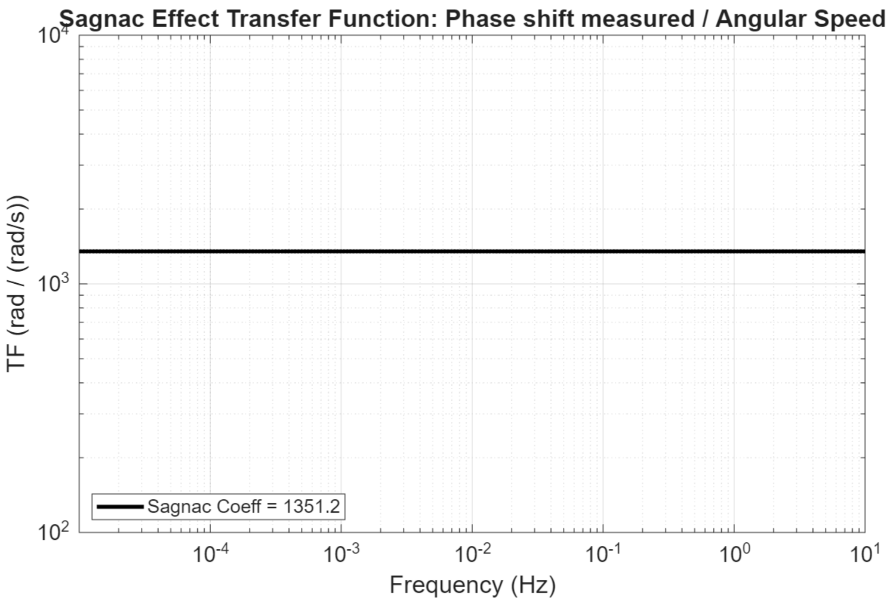

Figure 3.1: Sagnac Transfer Function Graph for FOG target specifications, using $L = 40e3\ m$, $D = 2.5\ m$ and $\lambda = 1550e-9\ m$

Moreover, compared to the beam balance sensor, one of the main advantages the FOG exhibits is the translational insensitivity. The alignment for the former is critical in order to minimize sensitivity to ground translation, whose contribution to the measured tilt scales with Mdg/I above the resonance frequency, where d is the misalignment, M the mass of the beam and I the inertia of the later. As seen in Figure, 3.2 for the best beam balance sensor, the sensitivity to translation is truly negligible (down to 10^{-4} $rad/(m/s^2\sqrt{Hz})$ with $d = 22$ nm). However, the others balance sensors reviewed in the state of the art present almost 3 orders more of magnitude in their CoM misalignments, bringing sensitivity to 10^{-1} $rad/(m/s^2\sqrt{Hz})$. This suggests that setting and controlling this parameter is not trivial, indeed, correcting it by sensor blending implies a high quality translational accelerometer and precise coupling modelling, introducing additional complexity.

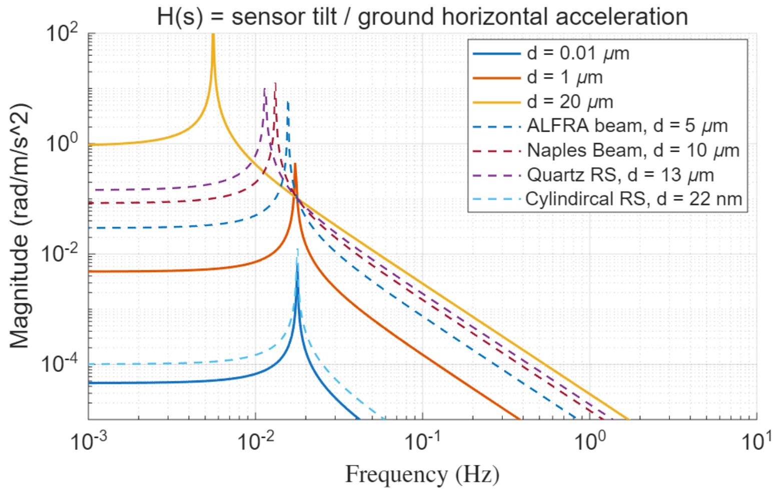

Figure 3.2: Transfer Function representing sensitivity to ground horizontal acceleration depending on the misalignment d with state of the art references.[1]

Third and last point, implementation and controlling complexity. For operation to stay constant and trustworthy, beam balance sensors require thermal stabilisation, remote CoM adjustment and a vibration-isolated environment. As shown in the Washington Beam Balance noise budget (Figure 2.5b), residual gas damping below 0.5 Hz left noise characterisation incomplete and unproven. On the other side, FOG requirements are not that demanding since is operationally far simpler and robust, with less mechanical high-precision tuning, proven by their transfer function comparison. It will be demonstrated in following sections, although their implementation is not without its own challenges.

3.1.2 FOG vs. Ring Laser Gyroscope

In the family of the optical rotation sensors, the RLG is the gyroscope who has achieved the highest resolutions. As mentioned before, the Gross Ring G at Wettzell achieves 10 $prad/(s\sqrt{Hz})$ between 1 and 10 mHz, and the Virgo implementation reaches 10 $nrad/(s\sqrt{Hz})$ below 1 Hz

[1]For the state of the art examples, just the misalignments are tuned, the rest of the parameters remain constant, therefore, functions are not fully representative.

with a 1.82 m arm [26].Their performance is really promising and it theoretically competes with FOGs of that size, however, the whether they can be integrated and efficiently deployed in the ET platforms is where the problem resides.

The first issue is the mechanical rigidity. An RLG structure needs to be highly calibrated and isolated from undesired vibrations and thermal gradients. Indeed, the optical cavity must sustain a round-trip perimeter that is an exact integer multiple of the laser wavelength to maintain resonance. Any mechanical deformation of the cavity walls, even at the nanometre scale, shifts this condition and injects spurious frequency noise directly into the beat signal. Therefore, an RLG cannot be trustfully implemented into a vibrating and flexible isolation platform since this delicate stability would be broken. In the Virgo observatory, the RLG is detached from the main platform, acting as an auxiliary rotation sensor in a nearby and customized controlled environment, designed to feedforward ground perturbations to main stage and not as feedback sensor. On the other hand, FOG are more flexible and insensitive optical path variations to higher extent [28].

The second issue is the lock-in. As mentioned in previous sections, under very subtle ground motion the sensor is blind. Backscattering between the counter-propagating beams causes the beat frequency to disappear and it cannot be overcome the same way FOGs surpass this obstacle, changing the optical source, since the inherent nature of RLGs signals require Lasers. Therefore, it must be avoided by mechanically "shaking" or dithering the cavity at several hundred Hz [11]. This vibration is an additional noise injected into a platform that must keep a mirror stable at nano-metric levels, compromising the performance of the system. On the other side, FOGs do not demand this technique since it has other ways to deal with Coherent Rayleigh Backscattering that will be reviewed in further sections.

3.1.3 Custom FOG vs BlueSeis3A

After establishing the technology approach for the gyroscope and justifying the reasons for it, it remains to argument whether to get the highest resolution FOG in the market or design it from scratch. The BlueSeis3A is the best commercially available IFOG in Europe in terms of noise and resolution. However, as shown in figure 3.3 , its noise floor in the frequency band of interest does not reach the target 10^{-10} $rad/(s\sqrt{Hz})$ required for ET isolation control, between 0.01 and 10 Hz. However, its limited resolution is partly due to its size constraints required for its application as a portable sensor.

In this case, the Sagnac scale factor is the highest representative. As it shows in the equation 3.1.1, the sensitivity is directly proportional to the product of LD, where L is the length of the fibre coil and D the diameter of the later, meaning that scaling the length and/or the diameter will scale proportionally the sensitivity. Therefore, compared to a commercial coil of a few dozen centimetres, a custom coil of 2 meters, which is the initial plan approximately, could be 1 or 2

[2] The LCG-Demonstrator, the liquid-based Eentec R1 and the Applied Technologies Associates (ATA)-smhd

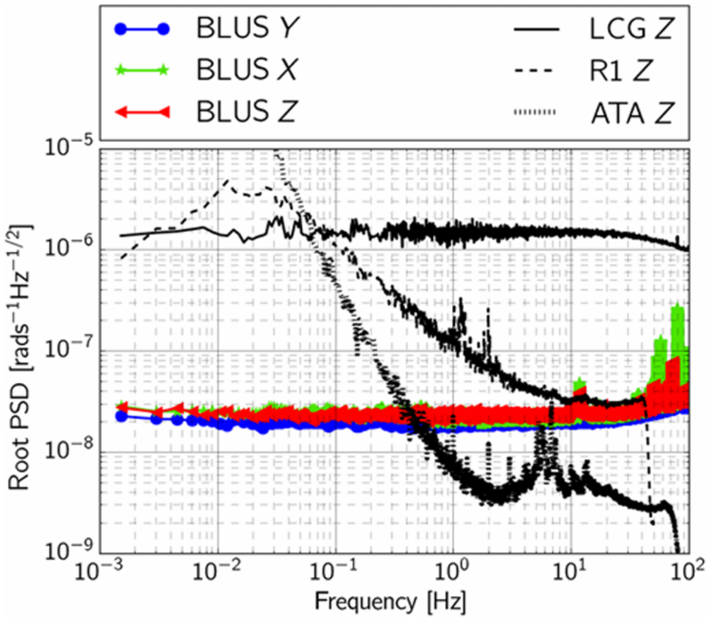

Figure 3.3: BlueSeis3A self-noise ASD along with other commercial seismometers [33].[2]

orders of magnitude more sensitive, due to the diameter and the inherent increase in length too. No commercial product is able to offer this so it must be custom modelled and manufactured.

Furthermore, leading the design and test of a custom sensor, allows more control and understanding of the noise sources of the system given the specific set of conditions. Consequently, the development of this custom FOG, the characterisation of its noise budget and the evaluation of its design in contrast of the ET requirements, are the main contribution of this thesis and are described in the following sections, starting from the simplest architecture into the most refined configuration.

3.2 Basic Configuration

The most simple Fibre Optic Gyroscope consists on a few elements to provide a measurement as shown in Figure 3.4. These are the following [10]:

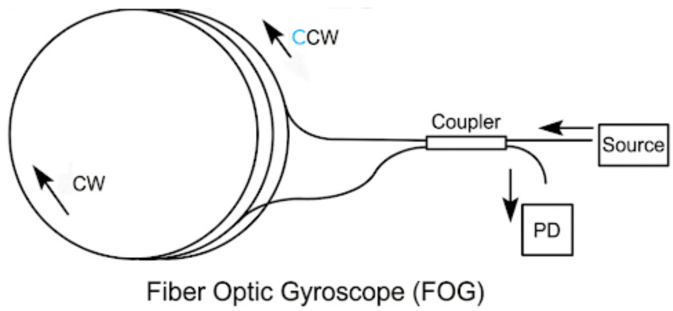

Figure 3.4: Mechanical and optical architecture of the simplest functioning FOG [10]

- Optical Source: Is the stable source that provides the measurement variable, injecting the light to the system through the fibre.
- Coupler: Guarantees the splitting of the light into two beams right before the fibre coil, making possible to compare the both path distances. Light is also redirected to the Photodiode through the same coupler or another one.
- Fibre Coil (FC): Represents the main optical journey (or trip) of the light, where clockwise (CW) and counter-clockwise (CCW) beams travel. Fibre Optic wires are enveloped around a cylinder (or coil) over metres to tenths of kilometres to achieve maximum sensitivity. It is mainly limited by the attenuation of the fibre.
- Photodiode (PD): Converts the intensity signal produced from the interference pattern into a electrical current. Then, is fed to the convenient devices to provide the digital output, providing human readable measurements.

As mentioned, light is split in the coupler into two identical beams that counter-propagate through the fibre coil and after, they recombine again at the same coupler. In the absence of rotation, the two optical paths are identical and the coupling takes place completely in phase, producing the maximum achievable intensity at the photodetector. In the case where the coil rotates over its main axis, the distance travelled by one beam is shortened as much as the other is lengthened, changing the phase at which the recombine again at the coupler. The phase shift $\Delta\phi$ is proportional to the angular speed Ω of this rotation. As mentioned before but for the sake of clarity, this is the Sagnac effect and is described by the following equation:

$$\Delta\phi_s = \frac{2\pi LD}{\lambda c}\Omega = \frac{8\pi NA}{\lambda c}\Omega \tag{3.2}$$

where L is the total fibre length, D the coil diameter, λ the wavelength of the light source, c is the speed of light in vacuum, N the number of turn and $A = \pi(D/2)^2$ the enclosed area per turn. On the other side, the intensity registered at the photodetector (I) is [11]:

$$I = I_0 \cos^2(\frac{\Delta\phi}{2}) = \frac{I_0}{2}[1 + \cos(\Delta\phi)] \tag{3.3}$$

where I_0 is the input intensity of the laser source (without considering fibre attenuation). This expression characterises the relation between the phase shift of the interference and the intensity readout through a cosine function.

Furthermore, a particularity of Fibre Optic Gyroscopes is its passive common-mode rejection. Since both counter-propagating beams travel the exact same distance and through the same environment (the fibre coil), every perturbation affecting both beams is subtracted from the final signal. In summary, the photodetector only reads the difference in phase shifts between beams, since Sagnac effect delays one wave and accelerates the other, these phase shift have different sign in the accumulated phase shift of each beam as explained in the equations below.

$$\Delta\phi = \Delta\phi_{CW} - \Delta\phi_{CCW}$$
$$\Delta\phi = (\Delta\phi_{Sagnac} + \Delta\phi_{Noise}) - (-\Delta\phi_{Sagnac} + \Delta\phi_{Noise})$$

However, if a perturbation disrupts the fibre coil, a phase shift will be induced in the light travelling through the coil. Typically, since both beams travel through the same features of the coil, the phase shift will be the same sign and magnitude for both, arriving at the photodetector at the same phase and rejecting that undesired noise. Only a truly non-reciprocal effect, which affects in distinct ways the counter-propagating beams, can produce a net phase shift at the output, such as the Sagnac effect. This feature inherently elevates the accuracy of the FOG architecture by simple reciprocity.

3.2.1 Noise Budget

Despite the natural common-mode rejection of the FOG architecture and its intrinsic insensitivity to translational motion, the noise floor of the simple configuration falls considerably short of the ET requirements. Figure 3.5 presents a simplified noise budget of this configuration, retaining only the dominant contributors for clarity. Two noise sources stand orders of magnitude above all others in the bandwidth of interest, and both will be thoroughly analysed and addressed in the following sections.

As observed in Figure 3.5, the noise floor is entirely dictated by two contributions: Coherent Rayleigh Backscattering (CRB) and Relative Intensity Noise (RIN), both sitting far above the ET target of 10^{-10} rad/s/$\sqrt{\text{Hz}}$.

CRB establishes a frequency-independent noise floor above roughly 0.3 rad/s/$\sqrt{\text{Hz}}$. It originates from microscopic inhomogeneities in the refractive index of the fibre core, which scatter a fraction of each propagating beam back in the opposite direction. With a narrowband laser source, these backscattered waves remain coherent with the primary beams and interfere with them at the coupler, producing a spurious phase noise that dominates the high-frequency end

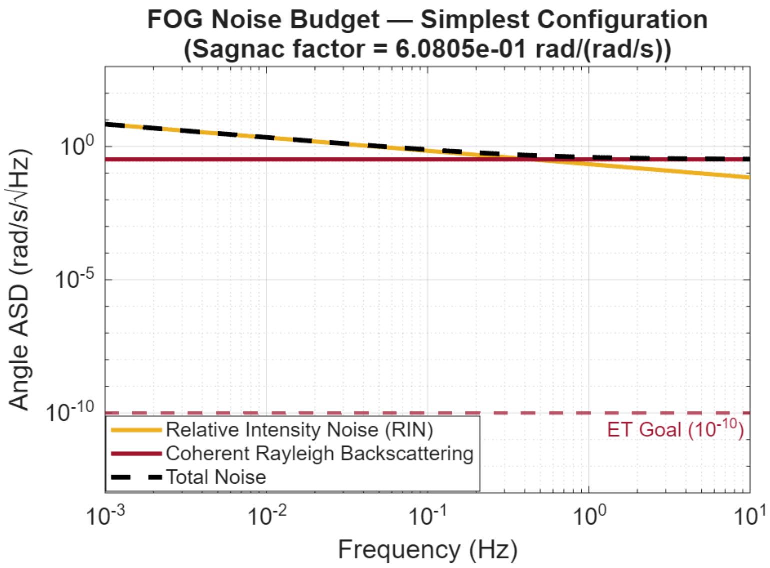

Figure 3.5: Simplified theoretical noise budget for the simple coil

of the band of interest.

RIN, by contrast, rises considerably towards low frequencies following a $1/f$ behaviour. No optical source emits a perfectly stable power output, and these intensity fluctuations propagate through the interferometer as a spurious phase shift unrelated to the Sagnac effect, dominating the noise floor across the low-frequency end of the band.

Together, CRB and RIN make the simple FOG configuration wholly inadequate for the ET isolation requirements. Their mitigation drives the most consequential architectural decisions discussed in the following sections.

3.3 Phase Modulator

As mentioned in the previous section, the simplest FOG produces an output intensity the follows a cosine function of the Sagnas phase shift. Looking again at equation , at very small rotation rates ($\Delta\phi \ll 1$) the measured intensity sits at the maximum of this cosine, since the first derivative term is 0, as it is demonstrated by the next equation:

$$I = \frac{I_0}{2}[1 + \cos(\Delta\phi)] \tag{3.4}$$

$$\frac{dI}{d\Delta\phi} = \frac{I_0}{2} sin(\Delta\phi) \tag{3.5}$$

Therefore, two problems arise. The first, when measuring very slow rotations, the approximation of the cosine states that the signal is proportional to the second order phase shift $\Delta\phi^2$, which for the ET isolation requirements the signal is completely buried by any noise floor. The second issue is that, at the maximum of the cosine, either $+\Omega$ or $-\Omega$ looks exactly the same, meaning that the instrument cannot differentiate between a clock or counter-clockwise rotation, as both can be observed in figure 3.6. Consequently, these two problems together, absurdly low sensitivity and sign ambiguity, arise from the reciprocal nature of optical path lengths in FOGs and interference.

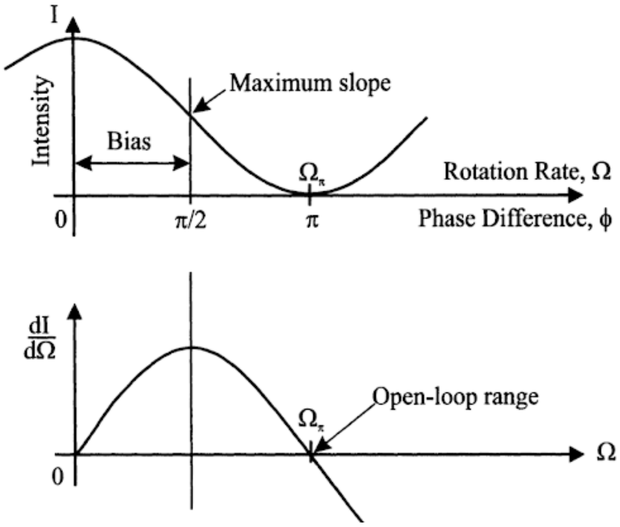

Figure 3.6: Top: Intensity readout depending on the phase difference of the interference. Bottom: Sensitivity in intensity to rotation rate [11].

The standard solution is to bias both beams into an initial phase shift, standing outside of the maximum of the cosine. However, it is not a trivial problem, since a phase delay cannot be applied passively in one direction and not in the other. Therefore, it is introduced a phase modulator into the optical path, which is an instrument that changes the refractive index of the optical medium, effectively slowing light. To avoid reciprocally phase shifting, the modulator is driven by a sinusoidal voltage varying phase like $\phi_m(t) = \phi_0 sin(2\pi f_m t)$, where ϕ_0 is the applied phase bias amplitude and f_m is the modulation frequency.

$$\Delta\phi_{total} = \Delta\phi + \frac{\phi_0}{2} sin(2\pi f_m t) \tag{3.6}$$

Then the equation of the intensity is:

$$I(t) = \frac{I_0}{2}[1 + cos(\Delta\phi + \frac{\phi_0}{2}(2\pi f_m t))] \tag{3.7}$$

Through the Jacobi-Anger identity, which is an specific identity for sinusoidal equations. The expression is developed into a form compound of factors of sine or cosine $\Delta\phi$ times sin or cosine $n \cdot 2\pi f_m t$ where n is equal to 1, 2, 3..., times the Bessel functions ($J_n(\phi_0)$), which are a family of harmonics for cylindrically symmetric problems. For the sake of simplicity, the first order approximation of the demodulated signal S is directly displayed below [34].

$$S \propto J_1(\phi_0) sin(\Delta\phi) \approx J_1(\phi_0)\Delta\phi \tag{3.8}$$

Then, to obtain the maximum signal the modulation amplitude must be $\phi = 1.84$ rad ($\pi/2$), at which J_1 reaches its first maximum [11]. At this point, the sensitivity is maximum and linear, for small phase shifts, and the response is not symmetrical any more, since the sign of $\Delta\phi$ is sensed through the slope of sensitivity.

Furthermore, the optimal modulation frequency is given by the transit time of the light through the coil $\tau = nL/c$, where n here is the refractive index. In one period τ, light entering the coil (CW f.e.) must experience one side of the modulation signal ($+\phi_0$ f.e.), whereas the beam exiting (CCW) must shift in the opposite way ($-\phi_0$). This is the definition of half wave, which means modulation frequency f_m must be:

$$f_m = 0.5 \cdot \frac{1}{\tau} = \frac{c}{2nL}$$

This way, the contribution of the phase modulator maximises the sensitivity, while interfering in the signal the least as possible. Finally, even for coils long as tens of kilometres, which is the industry maximum and it will be demonstrated in Chapter , the modulation frequency is of several kilohertz, standing significantly above of the ET isolation bandwidth and thus being easily separated from the rotation signal by demodulation.

3.4 Polariser & Interference

In order to have stable and coherent interference, two beams must come from the same source, physically interfere with a spatial difference smaller than the coherence length of the source, and share the same state of polarisation (SOP). Therefore, unpolarised light cannot interfere coherently, so FOGs will always require polarised light to work.

Optical fibre present a non-uniform refractive index cross-section [12]. This means, that depending on the orientation of the SOP, light will experience a different speed, where there is a preferential lane (fast axis; lower refractive index) and an orthogonal denser lane (slow axis; higher refractive index) experiencing a time delay, as observed in figure 3.7. In an ideal fibre with perfect cylindrical symmetry, these two lanes would be completely identical and propagation speed would always remain the same. In reality, manufacturing imperfections, bending, dynamic and accumulated mechanical stress changes unpredictably the refractive index, causing birefringence which is a small difference between two polarisation modes and often defined as $\Delta n = n_{max} - n_{min}$. Therefore, as polarized light propagates through the fiber coil, birefringence variations caused by mechanical and thermal perturbations induce coupling between polarization modes. As a result, the output state of polarization becomes highly sensitive to environmental fluctuations and may vary unpredictably over time, a phenomenon commonly referred to as polarization cross-coupling.

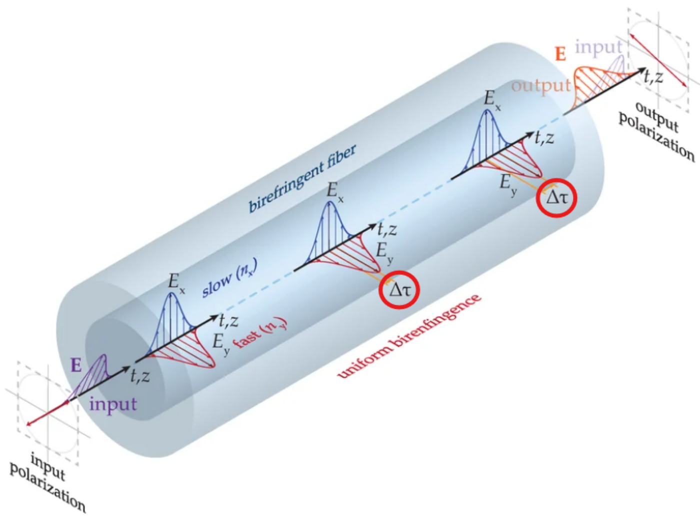

Figure 3.7: Scheme of light separated into two components and travelling through a birefringent optical fibre. Orthogonal components suffer a time delay due to the different refractive index, changing the state of polarisation along the fibre. [12]

The real consequence arises comes at the recombination of light. The signal at the output is properly defined only if the two beams share the same polarisation state, although they can still interfere as long as they share a common component. However, if the SOPs differ at recombination, only the common polarization component contributes to the interference signal, while the orthogonal component adds a constant intensity that carries no phase information. Consequently, the fringe visibility, which is [35]:

$$\mathcal{V} = \frac{I_{max} - I_{min}}{I_{max} + I_{min}} \tag{3.9}$$

is reduced below 1, where I_{max} is the intensity seen during a constructive interference and I_{min} is the intensity when the interference is destructive and ideally is 0. In the worst case, when the two beams present orthogonal SOPs, $I_{max} = I_{min}$ then $\mathcal{V} = 0$ and interference is impossible, a condition also know as polarisation fading. Furthermore, variations in the SOPs lead to fluctuations in fringe visibility and, consequently, in the effective scale factor K, since the amplitude of the detected interference signal is proportional to $\mathcal{V}$. A changing scale factor and a varying rotation rate are indistinguishable from each other, introducing a spurious noise particularly damaging at low-frequencies since these fluctuations are rather slow.

For this issue, the first solution is to introduce a polariser at input/output of the coil to define a preferential SOP and filter out the undesired modes, both at the entrance and the output. Additional solutions will be required and will explained in following sections. Only one polarisation mode is transmitted into the coil and the same is accepted at the output. This enforces the symmetrical nature of the FOG since both counter-propagating beams are forced to start the trip with the same polarisation state and to keep it at the point of interference, guaranteeing a stable signal over time and a properly defined fringe visibility.

Moreover, for further context, the polariser holds a extinction ratio, which is the ratio of the transmitted power in the preferential polarisation between the rejected polarisation defined in dB. For high performance applications, FOGs introduce polarisers of 60 to 80 dB of attenuation, meaning that the orthogonal polarisation mode transmitted is at least 6 orders of magnitude lower than the main signal [36].

3.5 Broadband Source & Coherent Rayleigh Backscattering

Coherent narrowband lasers are practical, powerful and precise, but they introduce a very significant noise which can have a dominant contribution to the overall noise floor of a FOG [37].

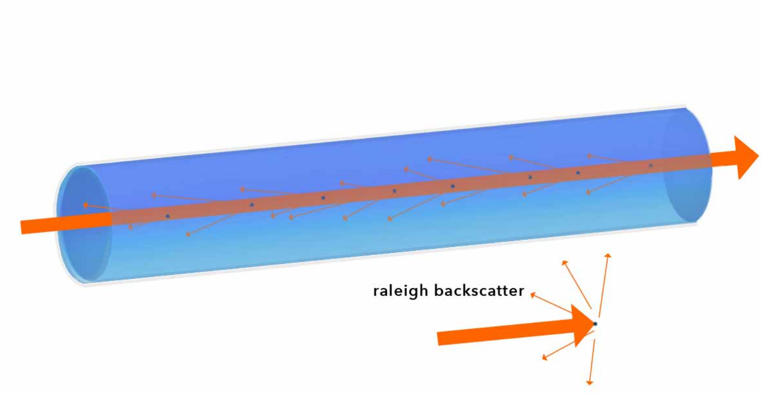

Figure 3.8: Scheme of the Rayleigh Coherent Backscattering process

When light propagates through an optical fibre, microscopic density fluctuations or any-sized imperfections in the glass continuously scatter backwards some fractions, this is called Rayleigh Backscattering. This phenomena by itself is unavoidable, since any possible refractive index gradient reflects light back, like in a Luneberg lens. However, the issue arises when the backscattered light interferes with the primary waves, specially at the recombination point in the coupler. Since the sources of wave backscattering are distributed randomly along the fibre, with a coherent laser source, the backscattered light is able to interfere with the main beam over long distances, increasing the noise proportionally. Furthermore, their relative phases fluctuate in their random distribution as environmental perturbations take place, producing a random walk in the phase output of the interferometer. Therefore, the longer the coherence length, the larger is this spurious phase noise, as it is represented below for the Amplitude Spectral Density (ASD) $\sigma^2_{\phi,bs}$ [38] [39]:

$$\sigma^2_{\phi,bs} = \frac{l_c \cdot \alpha_s \cdot S}{2\,\alpha_t}\left(1 - e^{-2\alpha_t L}\right) \tag{3.10}$$

where S is the backscattering coefficient of the fibre, l_c corresponds to the coherent length of the source and A_{eff} is the effective mode area. As mentioned, reducing l_c by several orders of magnitude would suppress this noise proportionally, greatly benefiting the noise floor of the FOG.

This noise mechanism is directly addressed by replacing the coherent laser with a broadband Amplified Spontaneous Emission (ASE) source, generally erbium-doped fibre ASE sources or SuperLuminescent Diode (SLD) are the favourite solutions in the industry. Their main feature is that light emission takes places over much larger bandwidths than laser sources, usually of tens of micrometers. Therefore, they present much shorter coherence lengths and effectively they diminish the Coherent Rayleigh Backscattering noise by several orders of magnitude.

To set a more intuitive context, the equations below describe how the coherence length is obtained. The following expression estimates it for a narrowband laser [40]:

$$l_c \approx \frac{c}{\Delta v} \tag{3.11}$$

where, v is the optic frequency of the optical source and Δv is the spectral bandwidth in Hz. Since $v = c/\lambda$, then deriving and approximating it turns to $|\Delta v| \approx c\frac{\Delta\lambda}{\lambda^2}$, where, λ is the central wavelength and $\Delta\lambda$ is the spectral bandwidth. When applying it to the previous equation the result is [40]:

$$l_c \approx \frac{\lambda^2}{\Delta\lambda} \tag{3.12}$$

which is more suitable for laser habitual characteristic features. An ultra-stable narrowband laser (f.e. the ADJUSTIK X15 model from Koheras) can have a linewidth Δv of 1 kHz [41]. On the other side an erbium-doped fiber ASE source (like the c-band OEM ASE source from OzOptics) has an spectral bandwidth $\Delta\lambda$ of 33 nm and a central wavelength λ of 1545 nm [42]. Applying these features to the corresponding equations, the narrowband laser shows a coherence length of 300 km whereas the broadband ASE source of 72 μm, exhibiting roughly 9 orders of difference.

In addition, ASE sources are generally less sensitive to temperature and vibration than narrow-linewidth lasers. Their spectral characteristics are primarily determined by the gain medium rather than by fluctuations in cavity length, which is very sensitive to environmental perturbation. While ASE sources exhibit lower coherence and poorer wavelength definition than single-frequency lasers, their reduced sensitivity to environmental perturbations makes them attractive for FOG applications. On the other side, the broadband source introduces an additional issue that the laser does not. Since the FOG scale factor depends inversely on the wavelength λ, seen in the Sagnac equation, the central wavelength must be very well defined and remain sufficiently stable to satisfy the accuracy requirements of the ET isolation platform, but thermal stabilisation required is actually less stringent than for laser cavities. This will raise an additional concern regarding the thermal environment but it should not demand a complicated thermal control, therefore sitting inside the list of reasons to control ET platforms environment.

3.6 Circulators and Isolators

In any FOG configuration there are several optical interfaces, such as connectors, couplers, splices, that reflect light back by its intrinsic nature on top of Rayleigh Backscattering. With a broadband ASE source, the backscattered light re-enters the gain medium of the optical source and interferes with the signal, perturbing its output power and frequency shape. This fluctuations propagate into the interferometer as intensity noise. Furthermore, after the intersection with the photodetector, reflected light can return through the coupler producing a DC background noise that reduces fringe visibility in the same way as the uncontrolled polarisation state mentioned before.

To address this problem, two complementary components are exposed. First, an optical isolator, which is an instrument, usually relying on the manipulation of the polarisation state, that easily transmits light in one direction, while strongly attenuation any light incoming from the opposite. It is placed right after the optical source to prevent even the most immediate backscattered light from perturbing the gain medium, protecting the source from additional intensity noise. The attenuation achieved is usually of 40-60 dB, which means a reduction of 4 to 6 orders of magnitude [36].

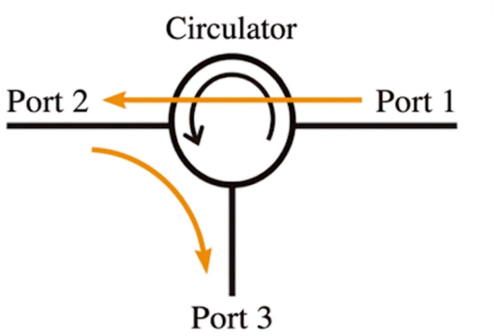

Figure 3.9: Optical circulator working concept [13].

Second, optical circulators are introduced. These devices, using Faraday rotators, are non-reciprocal optical components that typically feature three ports. Light entering port 1 is directed to port 2, while light entering port 2 is directed to port 3, as illustrated in figure 3.9. Any light propagating in the reverse direction is strongly attenuated ,effectively preventing light from coupling back into port 1. In FOG architectures, placing a circulator right at the intersection "optical source - coupler - photodetector" enables light to be redirected from the coupler (port 2) directly into the photodetector (port 3) without barely loosing optical power or disturbing further the source. This instrument simultaneously improves optical budget and further noise isolation of the source.

Furthermore, it is worth mentioning that isolators and circulators are thus sensitive to fluctuations in the polarisation state, since they actually work with embedded polarisers and waveplates to manage light circulation. Therefore, their implementation includes polarisation-wise measures to manage the orientation of the electromagnetic field.

3.7 Lyot depolariser & polarisation cross-coupling

As established in section 3.3, the interference signal intensity at the output directly the depends on the different accumulated phase shift and the extent to which the two counter-propagating beams share a common polarisation state. The polariser improved symmetry, interference and the rejection of the orthogonal mode noise contribution. However, it does not control what happens to the polarisation state inside the coil. Whether both SOPs are more or less perpendicular to the selected orientation, the signal can still fade if both beans are not aligned with the polariser axis, which is called polarisation fading. Therefore, the net polarisation state at the coil output is a contribution of the mechanical and thermal history of the fibre, which causes again a time-varying scalar factor due to random intensity fluctuations indistinguishable from a rotation signal.

In the end, this fluctuations are caused by polarisation cross-coupling, where the main wave progressively leaks into the orthogonal mode, slowing down as it propagates through the coil and eventually dissociating from the main carrier. Even with the polariser, both counter-propagating beams accumulate different polarisation evolutions due to the gyrotropic nature of the SOP, producing a non-reciprocal phase term.

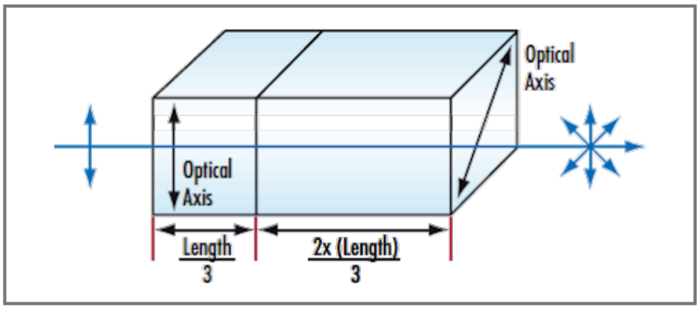

Figure 3.10: Lyot depolariser working concept [14].

The Lyot depolariser addresses these two issues, polarisation fading and cross-coupling, by ensuring that light entering the coil carries no defined polarisation, fostering an averaging across the polarisation spectrum and highly diminishing cross-coupling influence. This way, the polariser constantly filters out the same amount light, avoiding time-varying fluctuations in intensity. This depolariser consists of two sections of Polarisation Maintaining Fibre (PMF), which are fibre with two very different orthogonal refractive index or highly birefringent, spliced together with their polarisation axis tilted 45° from each other and the second segment twice longer. The strong birefringence causes the two polarisation components to quickly accumulate different relative phases. Since refractive index holds a second order dependency with frequency and broadband ASE source emits over a wide spectrum, different components of the wave will experience different phase shift, causing an uniformly distribution across the polarisation plane, and effectively depolarising light.

As a matter of fact, this mechanism relies on the broad spectrum of ASE source. A narrowband laser would not experience barely any depolarisation, since its spectral bandwidth is so short that the wave would follow the same polarisation route and end up just in a different polarisation state. As well, the intensity transmitted through the polariser is constant, but it also halved since half of the light's projection is in the orthogonal plane, which must be taken into account in the optical power budget.

Another alternative worth highlighting is the previously mentioned Polarisation Maintaining Fibre (PMF). Rather than scrambling the polarisation state, it suppresses cross-coupling by deliberately introducing a large birefringence, which creates a bigger energy gap that environmental perturbations are less likely to bridge. The mechanism is inducing a higher stress in one axis, generally through an elliptical-shaped core or the implementation of stress rods along the fibre. PMF architectures achieve really low levels of polarisation cross-coupling noise, making them common in high-performance commercial and custom instruments. However, their limitations makes them not yet a straight-forward choice for the fibre coil, although it will still be slightly used, so they will appear again discussed in subsequent sections.

3.8 Multifunction Integrated Optical Chip

On one side, the progressive introduction of components into the FOG architecture such as phase modulators, polarisers, couplers, circulators... introduce new splice points and interfaces, which contribute insertion loss, back reflection and even polarisation cross-coupling, specially regarding PMF splices. These losses are inherent to the process of implementation and profound system characterisations also include estimations of these measurements. On the other side, technology has evolved to develop instruments to cover several applications at the same time, improving performances and avoiding further losses.

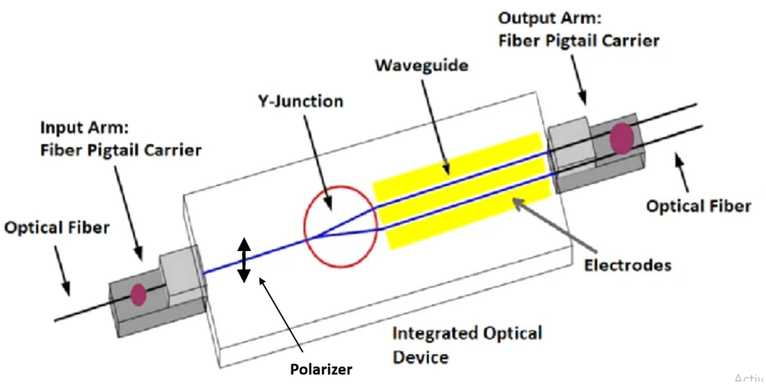

Figure 3.11: MIOC structure decomposition [15].

The multifunction integrated optical chip (MIOC or IOC) integrates several of the previously mentioned devices in one unit, typically created in a lithium niobate ($LiNbO_3$) substrate. Its structure implements, a waveguide polariser, a Y-junction beam splitter and electro-optic phase modulator in each arm. Light entering the chip from the pigtail is, first, polarised, achieving extinction rates of 60-80 dB usually as previously mentioned, then is equally split by Y-junction and, before reaching the two ends of the fibre coil, both beams are phase-modulated on each path by time-varying electrical field [15].

Looking specifically at each of the components, the waveguide polariser is fabricated directly into the LiNbO3 substrate, creating a waveguide that only supports propagation in one polarisation mode whilst the orthogonal axis radiates away. This extinction ratio is greater and more stable than those of discrete fibre polarisers. The Y-junction splitter is more precise due its creation process. Whereas standard fibre coupler are two fused fibres together, the Y-junction is fabricated in a single step on the same substrate and both arms are identical by design. Finally, the electro-optic phase modulator is implemented on each arm independently, allowing differential phase modulation between the two counter-propagating beams, which allows easier phase bias modulation, but most importantly, it applies the feedback ramp to maintain the $\pi/2$ phase bias. This technique consists on, rather recording the shift from the initial phase angle, measuring the applied voltage necessary to keep modulating the signal in close loop operation. This way, the interference continues to happen exactly at the desired phase bias $\pi/2$. This closed-loop approach not only maintains maximum sensitivity and preserves the sign discrimination between $+\Omega$ and $-\Omega$, but also extends the dynamic range of the FOG significantly beyond what open-loop detection allows.

Finally, is always an advantage for such characterisation and definition demanding systems to spare mechanical units, since additional mechanical degrees of freedom and resonances are avoided. Therefore, the architecture provides a better behaviour under vibrations and thermal drifts, and also spares the additional phase modulator necessary for symmetry.

3.9 Field-Programmable Gate Array Signal Processing

The optical signal arriving at the photodetector is a raw photocurrent encoding both the Sagnac phase shift and all noise contributions. Extracting the rotation rate with the required precision demands real-time demodulation, closed-loop phase control, and fast digital processing, which are tasks that must be performed simultaneously without degrading the instrument's noise floor. These requirements must be met by a competitive Field Programmable Gate Array (FPGA) which constitutes the digitally operational brain of the gyroscope architecture.

The first step after the optical wave arrives at the photodetector is the transmission from the optical power to photocurrent, performed directly by the photodiode. and immediately after, the current is converted into voltage through the Transimpedance Amplifier (TIA). The resulting signal is an interference pattern oscillating at the modulation frequency f_m, and whose amplitude encodes the Sagnac phase shift [43]. Then the signal is translated into the electronics by an analogue-to-digital converter (ADC), processed by a sampling rate significantly above the modulation frequency, habitually 100 times superior at least, to satisfy Nyquist criterion and avoid mixing the modulation signal with the Sagnac phase shift frequency (aliasing). The digital signal is then processed by the FPGA, going through the first demodulation. Knowing the value of f_m, the signal is then processed to retrieve back again the original optical signal and the actual phase shifts induced by the Sagnac effect, obtaining the sensed rotation of the platform.

FPGA will be working in closed loop for actively modulating the phase bias at the MIOC waveguide. From the information provided by the photodetector, the phase shift is obtained and auto-processed to implement the feedback to the phase modulator. Immediately after, the FPGA output is converted back into an analogue signal by a digital-to-analog converter (DAC) and routed to the MIOC phase modulator. This voltage is continuously adjusted in real time to generate an equal and opposite phase shift that cancels the Sagnac signal, keeping the interferometer locked at the $\pi/2$ bias point. It must be mentioned that the applied voltage resets to zero each time the accumulated phase shift reaches $\pi/2$, preventing the modulator from saturating. This reset must be precisely timed, as any discontinuity introduces a false phase shift that the system would misinterpret as a real rotation signal.

Beyond demodulation and closed-loop control, the FPGA also handles signal acquisition and drives any additional devices integrated into the system, such as reference photodetectors or auxiliary sensors. Centralising all these tasks in a single device minimises the processing latency, which is critical since high latency directly limits the upper frequency limit bandwidth of the active isolation control loop.

3.10 Winding Patterns and the Shupe Effect

As mentioned before, a fibre optic gyroscope measures rotation through the accumulated phase difference between the two counter-propagating beams inside the same coil. When they interfere back again at the beginning of the coil, the reciprocity of their paths produces a natural rejection of the perturbations that affected both beams equally. However, the common-mode rejection can only happen if the perturbation was experienced by the two beams at the same point, at the same time. In reality, both beams take their time to cross the same point of the fibre coil, since light has a finite speed and both beams start at both extremes of the fibre coil. Therefore, a time-varying perturbation, like a thermal fluctuation or a mechanical vibration, affecting a unevenly the coil will be experienced by the beams at different times, and the resulting phase shifts will not cancel exactly at the interference point. This is the Shupe effect, which was described by D.M. Shupe in 1980, and it is one of the most limiting and lingering noises even for FOGs implemented with modern corrections [**?**].

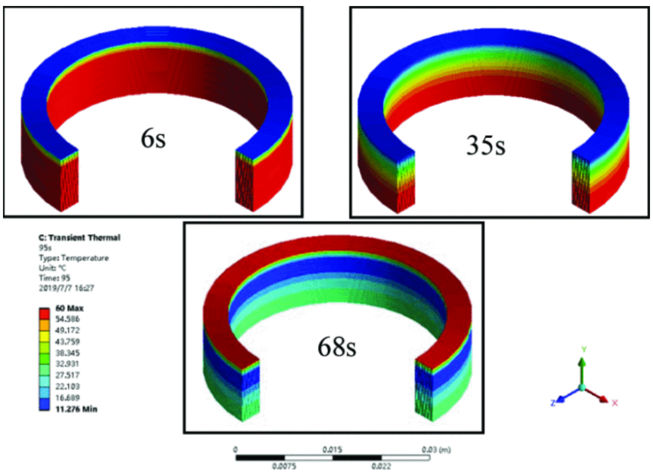

(a) temperature distribution at different times

Figure 3.12: Applied vertical thermal gradient to a fibre coil. Top: cooling cycle. Bottom: heating cycle [16].

The overall Shupe phase error can be derived by considering the phase accumulated by each beam as it travels through the fibre coil, where z is the distance to a point in the fibre and L is the total length of the fibre [17]:

$$\delta\phi_{Shupe} = \frac{2\pi n}{\lambda c} \int_0^L \dot{n}(z,t) \left(\frac{L}{2} - z\right) \cdot \frac{L-2z}{L} \, dz \cdot \Delta t \tag{3.13}$$

where $\Delta T^*(l,t) = [\Delta T(l,t) - \Delta T(l',t)]$ represents the temperature variation in contiguous segments of the fibre and $\alpha_{to} = dn/dT$ is the termo-optical coefficient. It can be observed that the weighting terms $(2l - L)$ are symmetric from the midpoint of the coil $z = L/2$, meaning that the areas closer to the middle contribute further less to the Shupe error, whereas the noise induced at the extremes contribute maximally. This issue represents the main motive for the winding pattern solution. If the fibre is arranged such that each segment located near one end has a corresponding segment near the other end, the same perturbation excites both symmetric segments at the same moment so recombining beams experience the same environment simultaneously and the noise induced is cancelled after, at the coupler.

The most used pattern in the industry is the quadrupole winding. Instead of simply winding the fibre from one end of the coil up to other, like a solenoid, the fibre is divided into four equal segments that are assembled in a specific sequence. From the middle of the fibre, the first half quarter is wounded in one direction and then, overlapping on top, the other half, after, the second quarter starts with the last sense of winding and completed with the opposite one, eventually assembling all four quarters, as represented in figure 3.13. This way, even inside the quarters themselves, are the distribution of the two halves of the fibre are alternative inside and outside the quarters. The result is that the fibre segments which are equidistant from the mid point are wound in adjacent layers and experiencing almost identical thermal and mechanical perturbations all the time. Therefore, the noise mitigation measure comes from the common-mode rejection mechanism represented by the Shupe integral rather than enforcing environmental uniformity.

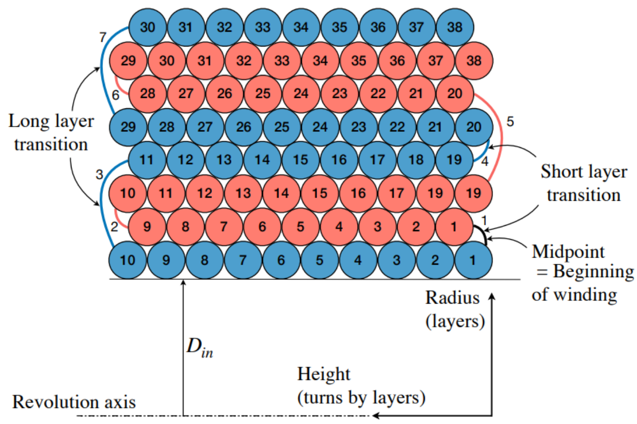

Figure 3.13: Cross section of a fibre coil assembled in with quadrupole winding. In blue: fibre wounded in one sense. In red: fibre wounded in the opposite. Numbers state the order of winding for each sense [17].

Furthermore, the quadrupole winding is the standard solution adopted by most resolution-concern manufacturers, including the commercial instruments mentioned before in chapter 2.1.2, like the Astrix 200 and the BlueSeis3A. Considering a fibre coil diameter of 2 metres as goal, this problem is particularly concerning since the coil physical size is makes more likely that spatial temperature gradients across its shape and more severe than in compact commercial units. In summary, the thermal management of the coil pushes the Shupe error down through the winding pattern choice, the appropriate thermal insulation and active temperature stabilisation if necessary, as such as the active feedback control for the seismic isolation.

3.11 Fundamental Noise Sources

The noises sources already addressed in the preceding sections like, polarisation fading, coherent Rayleigh backscattering, Shupe effect etc. can be improved with technical approaches, meaning that they come from imperfections in the optical, thermal or mechanical features of either the components or the environment, so they theoretically can be mitigated through careful engineering. However, the noises discussed in this section fall into a different section, there are three noises that represent this category. They arise from the physical laws of light and matter at the microscopic level and they settle the absolute floor below which no amount of engineering improvement can push lower the noise of the instrument. Therefore, is crucial to understand their origin and their driving factors for driving a further noise budget and achieve the best floor noises possible.

3.11.1 Shot Noise

Shot noise is a direct consequence of the non-continuum nature of light. An optical beam does not carry an uniform flow of energy but it transports it in very little discrete portions, called photons, which each has an energy hv where h is Planck's constant and v is the frequency of the photon. When the photodetector is illuminated by the beam, electron-hole pairs are generated when the photons are absorbed, producing an electrical current. However, the arrival of the photons at the detector acts as a random Poisson process even for perfectly stable light source, since the emission and the absorption of each photon is a statistic behaviour. These fluctuations at the photodetector are the shot noise [10].

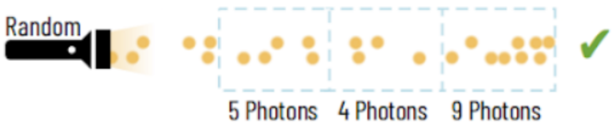

Figure 3.14: Representation of the shot Noise statistical nature [18].

Considering a mean photocurrent I_d at the detector, the power spectral density $PSD_{shot}(f) = 2eI_d$ is [44]:

$$PSD_{shot}(f) = 2e\bar{I}_d \tag{3.14}$$

where e is the electron charge. As observed, shot noise power is independent of frequency, resulting in a flat (white) noise floor across all frequencies. Its amplitude spectral density ASD_{shot} is:

$$i_{shot} = \sqrt{2e\bar{I}_d}$$

in units of $A/\sqrt{Hz}$ To understand this as a function of the rotation rate noise, the scale factor K of the instrument must be considered. The relation between the detected optical power P_d and the photocurrent is $I_d = \eta e P_d / hv$, where η is the quantum efficiency of the photodetector. Substituting and rewriting in terms of Sagnac phase shift noise:

$$\phi_{shot} = \frac{1}{\sqrt{P_d}}\sqrt{\frac{h\nu}{\eta}} \tag{3.15}$$

and then considering the sensitivity of the gyroscope, the equivalent noise floor due to shot noise is:

$$\Omega_{shot} = \frac{\lambda c}{2\pi NDA} \cdot \frac{1}{\sqrt{P_d}}\sqrt{\frac{h\nu}{\eta}}$$

From this equation several relevant conclusions can be drawn. In first place, shot noise decreases with increasing power at the photodiode as $1/\sqrt{P_d}$, which means that increasing the amount of photons provides better counting and reduces the relative fluctuation. Therefore, many efforts are invested in increasing the power input and optical power budget in the optical-based instruments. As well, every power loss in the system like, coupler splitting, instruments insertion, depolariser implementation... directly affects the shot noise floor. In second place, the coil area NA increases the sensitivity of the device, which reduces the denominator of the previous equation and the signal to noise ratio is improved. Therefore, a 2m diameter coil reinforces its strength as a valuable architecture choice, since coil area, fibre length and power are the only factors reducing this fundamental noise, although in following chapters it will be discussed how fibre length is not so obvious. In third and last place, since is a white noise, it sets an uniform noise floor across the entire ET control bandwidth without any frequency dependence.

3.11.2 Thermal noise

Thermal noise, also known as Jonhson-Nyquist noise when speaking of electronics circuits or thermomechanical noise, is produced by random motion of particles at any temperature above absolute zero. This noise is seen in two distinct ways, which are in the electronics of system, mainly in the detection chain, and in the optical fibre itself.

In the context of electronics, the transimpendance amplifier (TIA) which converts the photodetector current into a voltage introduces thermal noise according to the next equation [45]:

$$PSD_{Johnson}(f) = 4k_B T R_f \tag{3.16}$$

where $PSD_{Johnson}$ is the power spectral density, k_b is the Boltzmann constant, R_f is the resistance of the feedback resistor and T is the absolute temperature. On the other hand, the voltage resulting from the measurement at the photodiode V_{output} scales as $V_{output} = -I_d R_f$, where I_d is the photocurrent at the detector coming from the optical power, so the TIA R_f is the gain of the conversion. Then, introducing the amplitude thermal noise at the resistor $\sqrt{PSD_{Johnson}}$ as the output voltage, the result is the equivalent measured photocurrent to reach the thermal noise induced by the TIA itself, as the stated below:

$$i_{Johnson} = \frac{\sqrt{4k_B T R_f}}{R_f} = \sqrt{\frac{4k_B T}{R_f}} \tag{3.17}$$

Parallelly to the shot noise, the thermal noise at the amplifier follow a white noise behaviour along with a squared gain term at the denominator, meaning the trade-off between incrementing noise while incrementing the sensitivity is generally more favourable to the signal, increasing the resolution and pushing down the noise floor overall.

Furthermore, a high-resolution FOG is designed to operate in the regime dominated by shot noise, but requires the sufficient optical power at the photodetector to exceed the thermal noise of the amplifier. Regarding the detector, this would be the reasonable lower limit on the acceptable optical power and the upper bound would be stated by the saturation current.

On the other side, in the context of optic elements, thermal noise manifests as thermodynamic fluctuations in the refractive index of the fibre as part of the same microscopic atomic vibrations caused by the bare nature of temperature itself. These fluctuations are described by the fluctuation-dissipation theorem, which states that any physical system in thermal equilibrium manifests random fluctuations, varying its spectral density in proportion to the dissipation and the temperature. Since the light is partially absorbed by the fibre, this loss of optical energy is transferred into thermal energy changing the refractive index of the fibre, which is called thermal-optic coupling. Then, the power spectral densities of the local temperature fluctuations $S_{\delta T}$ [46]:

$$S_{\delta T}(\omega) = \frac{k_B T^2}{4\pi^2 L \kappa} \operatorname{Re}\left[\exp\left(-\frac{i\omega r_0^2}{2D}\right) E_1\left(\frac{i\omega r_0^2}{2D}\right)\right] \tag{3.18}$$

where k_B is the Boltzmann constant, T is the absolute temperature, L is the fibre length, κ is the thermal conductivity of silica, r_0 is the outer radius of the fibre, D is the thermal diffusivity of silica, ω is the angular frequency, and E_1 is the complex exponential integral function. However, these thermal fluctuations translate into phase shift noise through the next equation [46]:

$$S_{\phi}(\omega) \approx \frac{4\pi^2 L^2}{\lambda^2} \alpha_{TO}^2 S_{\delta T}(\omega) \tag{3.19}$$

where $\alpha_{TO} = dn/dT$ [1/K] is the thermo-optic coefficient of the fibre, which relates how thermal variations affect the refractive index. Then, the rest of the factors in equation 3.11.2 describe how fluctuations in n translate into phase delay across the entire fibre L.

It can be noticed that unlike both noises previously mentioned, thermal-optical phase noise is no longer white but frequency dependent. This frequency dependence arises from the asymptotic behaviour of the complex exponential integral $E_1(z)$ at low frequencies, producing a logarithmic spectral profile that closely resembles $1/f$ in the sub-Hz regime. This makes thermal-optical noise particularly relevant at low frequencies, precisely the most critical band for the seismic isolation of the ET. Furthermore, the longer the fibre L the more thermal fluctuations are given inside since each fibre segment contributes independently to the thermal phase noise, which is concerning since it also raises the Sagnac sensitivity. When estimating the optimal fibre length for the system, the both equations will be taken into account.

3.11.3 Relative Intensity Noise

Real optical sources do not emit perfectly stable light signals since the emission of photons is still a process driven by quantum statistics. Even after eliminating coherent noise mechanisms through the use of the broadband ASE source, the optical source emits fluctuations in the power output which causes spontaneous changes in intensity, undistinguishable from Sagnac induced phase [47].

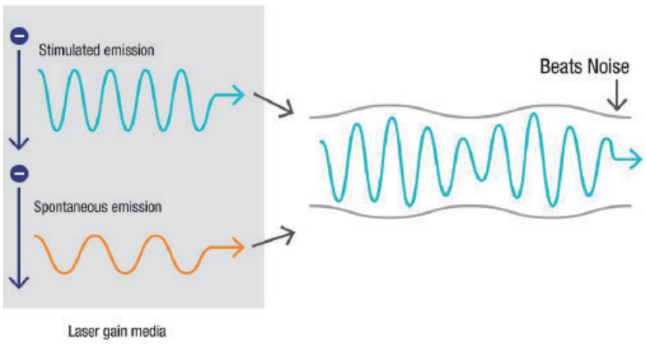

Figure 3.15: Two waves of different frequency and amplitude from the same gain medium adding together, causing fluctuations in intensity [19].

This is the Relative Intensity Noise (RIN) and is characterised by [48]:

$$RIN(f) = \frac{PSD_P(f)}{\bar{P}^2} \tag{3.20}$$

where $PSD_p(f)$ is the power spectral density of the power fluctuations and $\bar{P}$ is the mean power, then RIN is expresses in units of $1/\sqrt{Hz}$. Considering the responsivity of the photodetector is [49]:

$$\bar{I}_d = \mathcal{R}\bar{P}_d \tag{3.21}$$

where $\bar{P}_d$ is the mean power at the photodetector. After, looking at the generated photocurrent generated by RIN i_{RIN}, then, the same responsivity can be expressed as $i_{RIN} = \mathcal{R} \cdot \sqrt{PSD_p}$, and substituting the general mean power $\bar{P}$ by the mean power at the photodetector $\bar{P}_d$ inside the power spectral density of the power fluctuations, the equation is left like:

$$i_{RIN} = \bar{I}_d \sqrt{RIN(f)} \tag{3.22}$$

The main conclusion that can be drawn from here is that RIN scales up proportionally to $\bar{I}_d$, whereas shot noise grows with $\sqrt{\bar{I}_d}$, meaning that averaged through power input, the magnitude remains constant.

It can be pointed out that RIN in an ASE source has a dependency on frequency. It is relatively flat at high frequencies but rises towards lo frequencies due inner dynamics and other fluctuations, following a tendency of $1/f$ or $1/f^2$ profile below some few kilohertz typically. Consequently, the RIN spectrum of optical source must be very well defined and, often, actively suppressed with referential detection strategies of the source or with active power stabilisation, since the rotation signal of interest for the ET isolation platform is found below where the RIN starts to rise. As well, the previous expression is obtained assuming that tuning $\bar{P}_d$ is a free parameter, which is not real, since in practice, the detected power is limited by the optical source itself, the losses in the optical path, and the detector saturation. Therefore, is a useful reference but is not possible to implement in the real prototype.

The RIN is partially mitigated by the common-mode rejection effect provided by the Sagnac effect and the FOG architecture, since both counter-propagating beams originate from the same source, this power fluctuations is part of both beams and tend to cancel in the interference signal. However, mechanical and optical components are never perfectly created, and pose imperfections that leave residual RIN contribution significant enough to be included in the noise budget for the fulfilment of the ET requirements. These issues are related to the power evolution in the system, like not perfectly balanced 50/50 splitting ration or different power losses in both arms of the coil due to time-varying perturbations like vibrations. Consequently, manufacturing improvement is not enough to neglect this noise, but rather adding extra photodetectors for noise subtraction techniques and intensity correctors.

3.12 Relative Intensity Noise Subtraction

As mentioned in the previous section, RIN produces a current noise at the photodetector that grows with the detected power, and whose spectral density rises considerably towards low frequencies, which precisely the most critical band for ET isolation control. The common-mode rejection of the Sagnac architecture provides a partial natural mitigation, but as discussed before, the complete cancellation is only possible under conditions of perfect power splitting and symmetrical power losses in the two arms, in practice, are never fully achieved. A more robust approach to RIN suppression is therefore necessary.

The main and standard improvement to address this limitation is the implementation of a RIN subtraction scheme, which requires adding a tap coupler, typically a 95/5 or similar asymmetric splitter, immediately after the ASE optical source and before the circulator at the photodetector channel. This coupler separates a small fraction of the raw, unpropagated light and directs it into an additional photodetector, the reference photodiode [47].

Mathematically, the intensity of the optical source fluctuates over time such that $I_0(t) = \bar{I}_0 + \delta I(t)$, where $\bar{I}_0$ is the average intensity input and $\delta I(t)$ represents the RIN. However, in a realistic FOG architecture, correlating the main signal with the reference signal is not a trivial operation. The primary interferometric signal experiences significant optical attenuation across the system, due to fibre propagation losses, splice imperfections, and devices insertion losses, apart from the dynamic perturbations. Furthermore, it suffers from a considerable time delay $\tau = nL/c$, as it travels tens of kilometres through the fibre coil.

Consequently, the intensity measured at the main photodiode at time it arrives t reflects the source's state at a past time $t - \tau$. Both signals are therefore routed into the FPGA, where the reference is digitally delayed to match τ and normalised to account for the attenuation difference. The corrected signal is then obtained by subtracting the normalised reference from the main signal, cancelling their common RIN component while preserving the Sagnac phase shift.

In the sub-Hz band of interest, RIN fluctuations are slow enough that suppression ratios of 30–40 dB are achievable, pushing this noise source down significantly to facilitate meeting the ET requirements.

3.13 Other Noise Sources

3.13.1 Acousto-Optic Effect

The acousto-optic effect, which is also known as the photoelastic effect in the context of optical fibres, arises from the coupling between acoustic pressure waves and the refractive index of the fibre core. When an acoustic wave traverses the fibre, it produces a periodic mechanical strain in the glass, which changes the refractive index through the tensor relating the strain and optic faculties of the material, causing light to experiment different speeds along the fibre. For a silica fibre, the refractive index perturbation induced by a strain field ϵ is [50]:

$$\delta n = -\frac{n^3}{2} p_{eff}\epsilon \tag{3.23}$$

where p_{eff} is the effective strain-optic coefficient of fused silica, approximately 0.204 for standard single-mode fibre. The resulting phase perturbation accumulated by a the propagation of the beam through a referential fibre segment of length dz, which is affect by this refractive index change, is then:

$$d(\delta\phi) = \frac{2\pi}{\lambda}\delta n\, dz = -\frac{\pi n^3 p_{eff}}{\lambda}\epsilon\, dz \tag{3.24}$$

For a reciprocal perturbation, which is the one that is spatially uniform across the coil and constant in time, both counter-propagating beams accumulate identical phase shifts. The effect cancels at the interference point by exactly the same reason as for any other common-mode perturbation, either caused by vibrations, thermal gradients or optical imperfections. The acousto-optic effect becomes a noise source only when the acoustic field is not uniform across the coil or varies in time, then it breaks the conditions for reciprocal cancellation by the same mechanism discussed for time-varying losses in the previous section. It is worth noting that, despite its name, the dominant source of acousto-optic noise in this context is not airborne sound but rather mechanical stress waves propagating through the fibre coil from the vibrating isolation platform itself. This distinction is relevant because it implies that acoustic isolation of the coil from the surrounding air, whilst beneficial, is secondary to the mechanical decoupling of the coil from the platform structure.

In practice, acoustic noise in the environment of a gravitational wave detector describes a wide frequency range and is spatially non-uniform, especially for a 2 m diameter coil whose physical extent is comparable to the wavelength of audible acoustic waves. Therefore. different segments of the coil are subject to different strain amplitudes for each moment in time, and the integral over the coil, which is similar to the Shupe noise, does not cancel. The resulting phase noise contribution can be expressed as [50]:

$$\delta\phi_{acoustic} = \frac{\pi n^3 p_{eff}}{\lambda}\int_0^L \delta\epsilon(z,t)\left(\frac{L}{2} - z\right) dz \tag{3.25}$$

where the symmetric driving term $\left(\frac{L}{2} - z\right)$ is the same as in the Shupe effect, demonstrating a consequence of the identical physical origin of the two phenomena. It can be highlighted that the quadrupole winding pattern introduced in section therefore provides partial mitigation of the acousto-optic noise by the same geometric cancellation as for the thermal perturbations, since adjacent fibre layers experience similar acoustic strain fields, as thermal gradients, and their contributions to the integral partially cancel.

The remaining acousto-optic noise after quadrupole winding depends on the dimensions of the acoustic field across the shape of the coil. For acoustic wavelengths much larger than the coil diameter, which are at frequencies below approximately $c_{sound}/2D \approx 170$ Hz for the 2 m target architecture in question, the field is nearly uniform across the coil and the cancellation is effective. At higher frequencies, where the wavelength becomes similar or smaller than the coil dimensions, the spatial non-uniformity increases and the residual noise grows. The primary mitigation after applying the winding pattern is acoustic isolation of the coil through protection of a mechanical case to damp vibrations, and careful site selection to minimise the influence of the acoustic environment, which are both inherent to the ET project.

3.13.2 Faraday Effect

The Faraday effect is the rotation of the polarisation state of light propagating through a medium under the influence of a magnetic field and parallel to the propagation direction. In an optical fibre, the Faraday rotation accumulated θ_F over a length dz in such magnetic field $B_{\parallel}$ [51].

$$d\theta_F = V_V B_{\parallel}\, dz \tag{3.26}$$

where V_v is the Verdet constant of the fibre material, which is approximately 4.68×10^{-6} rad A^{-1} for fused silica at 1550 nm. The total Faraday rotation accumulated over the full fibre length is then [51]:

$$\theta_F = V_V \int_0^L B_{\parallel}(z)\, dz \tag{3.27}$$

The Faraday is an effect non-reciprocal by nature. It is gyroscopic or sense dependent effect, meaning that a beam propagating in one direction accumulates a rotation $+\theta_F$ whereas a beam propagating in the opposite direction accumulates $-\theta_F$, meaning the rotations add up instead of cancelling. This is precisely the behaviour of a defined and non-reciprocal phase perturbation in the Sagnac interferometer, and it is what makes the Faraday effect a genuine noise source from the beginning rather than a noise suppressed by common-mode rejection.

Between the CW and CCW beams, the non-reciprocal phase shift introduced by the Faraday effect can be related to the polarisation rotation through the Jones matrix convention, which are matrixes that describe the weight of the polarisation components for a light vector defined this way. For a linearly polarised input and a small Faraday rotation, the spurious phase shift is is proportional to θ_F and produced by $\Delta\beta$ the linear birefringence difference, which corresponds to the refractive index difference between the slow and the fast axis, t is the twist rate of the fibre, which represents how refractive axis rotate along the fibre due to machining procedures. Therefore, to the integral of the longitudinal magnetic field along the fibre as [51]:

$$\delta\phi_{Faraday} \propto \frac{4Vt}{\Delta\beta}\int_0^L B_{\parallel}(z,t)\,dz \tag{3.28}$$

As observed in the previous equation, the time-varying magnetic, sourcing from the electromagnetic actuators of the isolation platform, from power supply ripple, or from external sources, produces a time-varying false phase shift that directly mimics a rotation signal. For a 2 m coil of total fibre length L in the magnetic environment of an active isolation platform, this contribution must be carefully evaluated, since dimensions might make corrections difficult in this scenario.

The standard mitigation is magnetic shielding of the coil. It is a high-permeability enclosure, typically mu-metal, which can achieve permeability values of 10^4-10^5 compared to open spaces, working by diverting the external magnetic flux around the coil, reducing the field inside by the same factor as the permeability of the shielding material. For typical isolation magnetic environments and the Verdet constant of silica, a single layer of mu-metal shielding is generally sufficient to suppress the Faraday noise below the shot noise floor. It can be remarked that the shielding enclosure also contributes to the acoustic isolation of the coil discussed in the pervious section, since it partially damps incoming vibrations, making it a dual-purpose component in the instrument design.

3.13.3 Optical Kerr Effect

The FOG architecture must deal with non-linear optical phenomena, beyond environmental disturbances like acoustics and magnetic fields. The most representative of these is the Optical Kerr Effect, a non-linear process where the refractive index of the silica fibre becomes dependent on the intensity of the light propagating through it. Concretely, is the product of the third-order term in the refractive index of fused silica, causing intensity fluctuations to produce phase shifts unrelated to rotation. Then, in a standard single-mode fibre, the refractive index can be expressed as [52]:

$$n(I) = n_0 + n_2 I \tag{3.29}$$

where n_0 is the linear refractive index, $n_2 \approx 3 \times 10^{-20}\ m^2W^{-1}$ is the refractive index coefficient of third order of standard single-mode fused silica fibre, and I is the local optical intensity in W m^{-2}

Further more, light is an electromagnetic wave, and when a high-intensity optical source is projected through the tiny core of a single-mode fibre, its concentrated electric field physically distorts the electric configuration of the silica matrix. This distortion locally increases the refractive index of the glass for the time a wavepacket passes through it. Consequently, the apparent refractive index is higher and the beam slows itself down, which is a phenomenon called as Self-Phase Modulation (SPM). Simultaneously, this altered refractive index also slows down the counter-propagating beam crossing that segment of the fibre, which is known as Cross-Phase Modulation (XPM).

In practice, cross-phase modulation is inherently twice as strong as self-phase modulation. Then, considering power distribution, the Y-junction of the MIOC splits the optical power exactly equally (50/50) in a perfectly ideal FOG. Consequently, the clockwise (CW) and counter-clockwise (CCW) beams pose identical intensities, introducing an identical change in the refractive index, which in this case is the Kerr effect. As a symmetrical effect, it cancels out upon recombination. However, in practice, manufacturing tolerances dictate that true 50/50 splitting is impossible. If the MIOC splits the power asymmetrically by a tiny fraction, like a 49.99/50.01, the CW beam will have a slightly different power P_{CW} than the CCW beam P_{CCW}.

This power asymmetry causes the two beams to experience slightly different refractive indices and fosters that difference between SPM and XPM, consequently travelling at different speeds and accumulating a non-reciprocal phase shift over the length of the fibre L. The resulting Kerr-induced phase error $\Delta\phi_{Kerr}$ is proportional to the power difference [53]:

$$\Delta\phi_{Kerr} = \frac{4\pi L n_2}{\lambda A_{eff}}(P_{CW} - P_{CCW}) \tag{3.30}$$

where A_{eff} is the effective mode area of the fibre core and λ is the main wavelength of the optical source. Even a 0.1% splitting asymmetry can introduce a false rotation signal capable of drowning out the signal of massive cosmic events, specially considering such long fibre coil and a highly sensitive application like the ET. However, the utilization of the previously introduced broadband Amplified Spontaneous Emission (ASE) source, which was initially selected to mitigate Coherent Rayleigh Backscattering, provides a powerful solution to the Kerr effect as well. The Kerr phase shift is strictly dependent on the intensity fluctuations of the optical source. Therefore, for a highly coherent and monochromatic laser, the Kerr error follows the equation above. On the other hand, an ASE source presents quantum and thermal light statistics, where the intensity fluctuates randomly over a wider spectral bandwidth favouring the averaging of this phenomena, just as with the RIN.

When the wavepacket interacts with the glass to affect itself (SPM), since the ASE light is highly fluctuating, these localized high-intensity spikes mathematically mix, effectively doubling the intensity of the Self-Phase Modulation. Meanwhile, because the CW and CCW beams are strongly uncoherent, their chaotic spikes do not add when they cross paths, leaving the Cross-Phase Modulation unaffected. By doubling just the SPM, the chaotic nature of the ASE source balances it with the naturally stronger XPM, displacing this fluctuation to a symmetrical phenomena that is rejected at the natural recombination of the FOG. Then, this statistical feature compensates the induced phase shifts by the Kerr effect for both directions, diminishing significantly the possible non-reciprocal intensity fluctuation augmented by the Optical Kerr Effect.

3.14 Final Fibre Optic Gyroscope Architecture

Throughout all the problems assessed and the solutions provided in the preceding sections, this section presents the assembly of the final FOG architecture. To remind the reader of the starting point, the simplest operational FOG configuration is shown again in Figure 3.16, consisting of only an optical source, a coupler, a fibre coil and a photodetector [10].

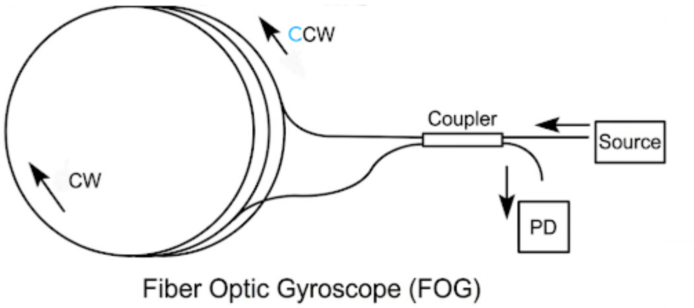

Figure 3.16: Mechanical and optical architecture of the simplest functioning FOG

This minimal configuration, whilst functional, falls critically short of the performance demanded by the Einstein Telescope. Its main limitations are the low sensitivity and sign ambiguity at near-zero rotation rates, the susceptibility to polarisation fading, and a noise floor dominated by Coherent Rayleigh backscattering and Relative Intensity Noise. These problems alone already place the simple FOG several orders of magnitude above the ET target resolution of 10^{-10} rad/s/$\sqrt{\text{Hz}}$ in the band of interest between 10 mHz and 1 Hz. Beyond these primary limitations, a thorough noise analysis revealed additional contributions, namely the Shupe effect, polarisation cross-coupling, the Optical Kerr Effect, the Faraday effect and acousto-optic noise, each of which required a dedicated architectural solution. The instruments introduced to address all these noise sources are summarised in Table 3.1.

Table 3.1: Summary of implemented instruments in the final FOG architecture.

Instrument	**Description**	**Problem mitigated**
Phase modulator (MIOC)	Sinusoidal phase bias applied at $f_m = c/2nL$, shifting the operating point to maximum sensitivity	Low sensitivity and sign ambiguity at near-zero rotation rates
Polariser (MIOC)	Waveguide polariser with 60–80 dB extinction ratio enforcing a single polarisation state at coil input and output	Polarisation fading and fringe visibility fluctuations

Continued on next page

Table 3.1 – continued from previous page

Instrument	**Description**	**Problem mitigated**
Y-junction splitter (MIOC)	Lithium niobate integrated splitter guaranteeing a symmetric 50/50 split	Kerr-induced spurious phase shifts from power asymmetry
Broadband ASE source	Broadband source with coherence length of tens of μm, orders of magnitude shorter than a narrowband laser	Coherent Rayleigh Backscattering; Optical Kerr Effect
Lyot depolariser	Two PMF segments spliced at 45° in a 1:2 length ratio, scrambling polarisation across the ASE spectrum	Polarisation cross-coupling and fading inside the fibre coil
Optical isolator	Component placed after the ASE source attenuating back-propagating light by 40–60 dB	Optical feedback into the gain medium
Optical circulator	Three-port non-reciprocal device redirecting the returning signal directly to the photodetector	Power loss at the source-detector junction; source feedback noise
Reference photodetector & RIN subtraction	Tap coupler sampling raw source output; reference digitally delayed and normalised in the FPGA before subtraction	RIN, particularly its $1/f$ rise below 1 kHz
Quadrupole winding	Four fibre segments wound alternately so sections equidistant from the midpoint lie in adjacent layers	Shupe effect; acousto-optic noise
Magnetic shielding	Mu-metal enclosure reducing the internal magnetic field by 10^4–10^5	Faraday effect from actuator and power supply fields
FPGA	Real-time processor handling demodulation, closed-loop phase ramp, RIN subtraction and data acquisition	Signal extraction; dynamic range extension

It is worth noting that several of these solutions are not independent additions but rather interconnected design choices that simultaneously address multiple noise mechanisms. Most notably, the broadband ASE source, selected primarily to suppress Coherent Rayleigh Backscattering, also provides the wide spectral bandwidth required by the Lyot depolariser to function and naturally mitigates the Optical Kerr Effect through its incoherent photon statistics. Similarly, the mu-metal magnetic shielding enclosure that strongly suppresses the Faraday effect. This interconnected nature of the design choices reflects the complexity of building a high-precision instrument at this performance level. The complete implementation of all these instruments leads to the final FOG architecture of this thesis, represented in Figure 3.17

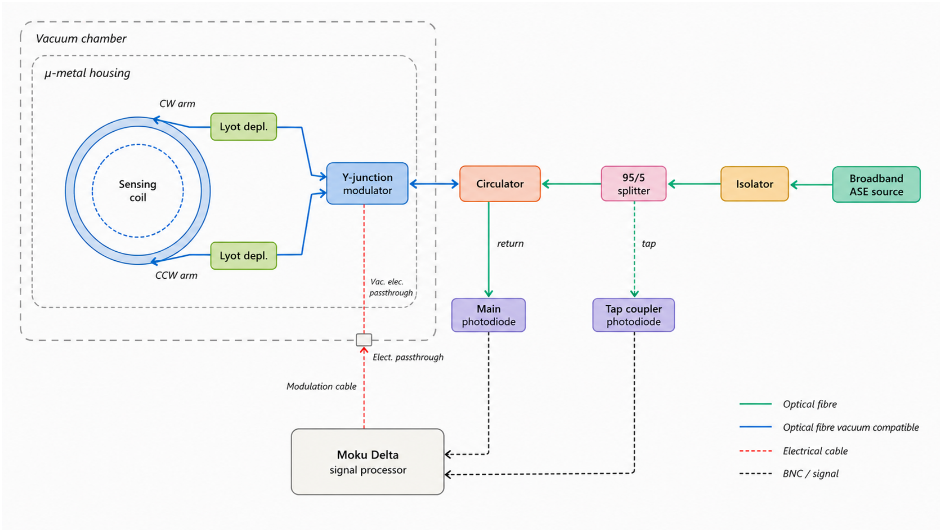

Figure 3.17: Final architecture scheme for the developed fibre optic gyroscope [20]

The transition from the simple to the final architecture follows two logical steps: the substitution of the original components for higher-performance equivalents, and the introduction of entirely new elements targeting the noise sources identified in the preceding sections.

Regarding the source and splitting stage, the narrowband laser is replaced by a broadband erbium-doped ASE source, whose short coherence length suppresses Coherent Rayleigh Backscattering and naturally mitigates the Optical Kerr Effect. Immediately after, an optical isolator prevents any back-propagating light from re-entering the gain medium. The splitting and polarising functions, previously handled by a simple coupler, are now performed by the MIOC, which integrates a waveguide polariser, a Y-junction splitter and two electro-optic phase modulators in a single lithium niobate substrate. The Y-junction guarantees a symmetric 50/50 split, the waveguide polariser enforces a well-defined state of polarisation (SOP) at the coil input, and the phase modulators drive the interferometer at the $\pi/2$ bias point of maximum sensitivity, resolving both the sign ambiguity and the low-sensitivity problems of the simple configuration. An optical circulator placed at the MIOC output port redirects the returning interferometric signal directly to the main photodetector, recovering the optical power that would otherwise be lost.

Regarding the coil stage, a Lyot depolariser is placed at each arm of the MIOC, ahead of the fibre coil. Although a single depolariser is the standard approach to prevent polarisation fading, the symmetric placement of two depolarisers ensures that both counter-propagating beams enter the coil with the same scrambled SOP, enhancing common-mode rejection of any polarisation noise accumulated during propagation. The fibre coil itself is wound in a quadrupole pattern, so that segments equidistant from the midpoint lie in adjacent layers, providing the geometric cancellation at the heart of Shupe and acousto-optic noise suppression. The coil, the MIOC and the depolarisers are enclosed in a μ-metal housing, which shields the fibre from external magnetic fields. In vacuum operation, this assembly would sit inside the vacuum environment directly.

Regarding the detection and signal processing stage, a 95/5 tap coupler placed immediately after the isolator redirects a small fraction of the raw source output to a reference photodetector. Both photocurrents are converted to voltage by transimpedance amplifiers (TIA) and routed to the FPGA, which performs synchronous demodulation at f_m, applies the digital delay and normalisation required for RIN subtraction, and feeds back the closed-loop phase ramp correction to the MIOC modulators to maintain the $\pi/2$ bias point at all times.

Chapter 4

Results and discussions

4.1 Final Noise Budget

The comparison between the simple FOG configuration and the final FOG architecture is performed through the discussion of their corresponding noise budgets. Supporting on the equations provided in previous sections, the noises are represented in figure 4.1 and figure 4.2.

Furthermore, for the better addressing the comparison, two other aspects are evaluated. Since the simple FOG resembles the simplest prototype that can be tested, the parameters of the fibre coil differ from the final version, as shown in table 4.1, changing the resolution factor of the gyroscope (K_S):

Table 4.1: Fibre coil parameters comparison between the simple and final FOG configurations.

Parameter	**Simple FOG**	**Final FOG**
Diameter D (m)	0.45	2.5
Fibre length L (km)	1	20
Sagnac coefficient K_S (rad$\cdot s/rad$)	6.08×10^3	6.76×10^5

On the other side, the most relevant noises will be addressed through the comparison of the optical sources of each configuration, as represented in table 4.2. However, part of their weight is caused by the RIN contribution of each and the information for the broadband ASE source was obtained experimentally from a similar optical source.

As observed in Figure 4.1, the simple FOG noise budget is completely dominated by two sources across the entire frequency band of interest: the Relative Intensity Noise (RIN) and the Coherent Rayleigh Backscattering (CRB). Both are direct consequences of using a nar-

[1] Narrowband laser specifications from [41] and Broadband ASE source specifications from [42]

Table 4.2: Comparison of the optical source parameters between the simple and final FOG configurations.

Parameter	**Simple FOG**	**Final FOG**
Source type	Narrowband laser [1]	Broadband ASE
Central wavelength λ (nm)	1550	1550
Spectral bandwidth $\Delta\lambda$ (nm)	8×10^{-9}	33
Coherence length l_c	$\sim$300 km	$\sim$72 μm

rowband coherent laser source, whose long coherence length usually ranges from hundreds of metres to hundreds of kilometres. The RIN presents a $1/f^{1/2}$ dependence, reaching values above 10^{-1} $rad/s/\sqrt{Hz}$ at 10^{-3} Hz and approaching the CRB floor near the same frequency. In contrast, the CRB, constitutes a flat white noise floor around 10^{-1} $rad/s/\sqrt{Hz}$, completely independent of frequency, due to its statistical nature. Together, these two sources set the total noise (dashed line) between nine and ten orders of magnitude above the ET requirement of 10^{-10} $rad/s/\sqrt{Hz}$, making the simple configuration entirely inadequate for the target application.

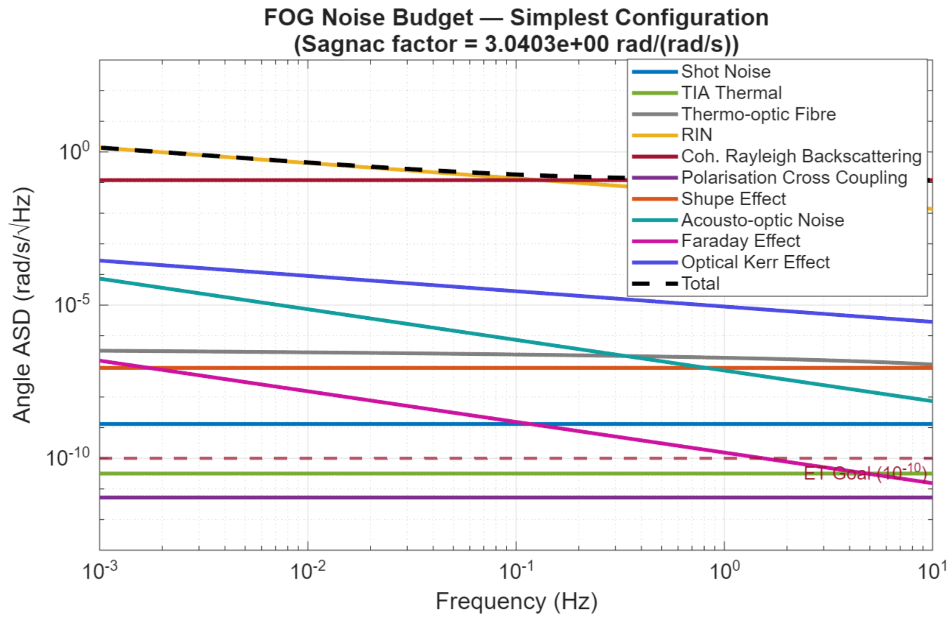

Figure 4.1: Theoretical noise budget of the **simple** FOG configuration

Below these dominant contributions, a second group of noise sources sits mostly between 10^{-4} and 10^{-9} $rad/s/\sqrt{Hz}$. The Optical Kerr Effect is the highest of these, reaching approximately 10^{-3} $rad/s/\sqrt{Hz}$ at 10^{-2} Hz and decreasing as $f^{1/2}$ towards higher frequencies, which is caused directly by the RIN(f) dependence in its expression. Immediately below it, the acousto-optic noise shows a steeper $1/f$ decay, crossing below 10^{-8} $rad/s/\sqrt{Hz}$ above 1 Hz, proportional to the reference acceleration profile for the bandwidth of interest ($1/f$), but considerably high towards lower frequencies. The Shupe Effect and the thermo-optic fibre noise appear as flat contributions around 10^{-8} and 10^{-6} $rad/s/\sqrt{Hz}$ respectively, the later presenting slow logarithmic decay and both reflecting thermodynamic fluctuations intrinsic to the fibre material. The Faraday Effect, driven by the ambient magnetic field ASD, presents a $1/f$ profile decreasing from almost 10^{-7} $rad/s/\sqrt{Hz}$ at 10^{-3} Hz and crossing the ET goal near 1 Hz.

Finally, the two lowest noise contributions, which are TIA Thermal (Johnson-Nyquist) and Polarisation Cross Coupling, sit at or below the ET requirement across the band of interest, with TIA Thermal both flat around 10^{-10} $rad/s/\sqrt{Hz}$, and the Polarisation Cross Coupling below 10^{-11} $rad/s/\sqrt{Hz}$. This confirms that the fundamental limits of the instrument are not just the issue themselves, but the problem lies considerably in the optical and environmental noise sources that the simple configuration does nothing to suppress.

Regarding the final FOG noise budget, shown in Figure 4.2, the implemented architecture has consistently pushed all noise contributions downward. Nevertheless, the same two noise sources continue to dominate the noise floor: RIN and Coherent Rayleigh Backscattering (CRB). Their relative behaviour follows a similar pattern to the simple configuration, with RIN dominating at low frequencies, reaching 10^{-5} rad/s/$\sqrt{\text{Hz}}$ at 10^{-3} Hz, and gradually approaching the CRB level above 1 Hz. The broadband ASE source has suppressed both contributions by approximately five orders of magnitude through its effect on the RIN spectral profile and the dramatic reduction in coherence length, yet the noise floor in the band of interest remains limited to $\sim 10^{-6}$ rad/s/$\sqrt{\text{Hz}}$.

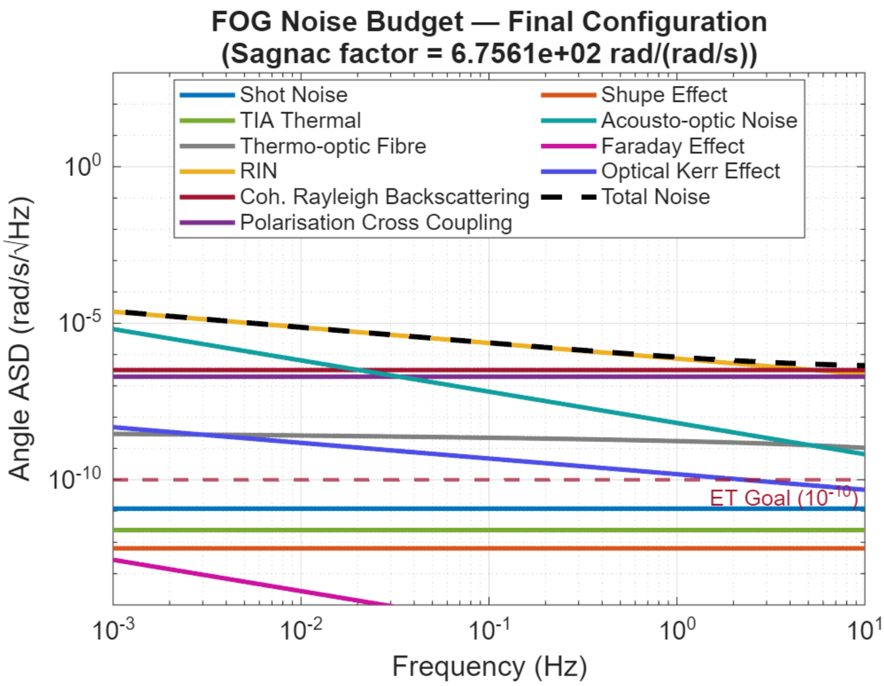

Figure 4.2: Theoretical noise budget of the **final** FOG configuration

Beyond these two dominant contributions, the acousto-optic noise and polarisation cross-coupling sit close to the current noise floor and merit attention. The acousto-optic noise takes over as the leading contribution below 10^{-3} Hz, but falls steeply with frequency, reaching 10^{-7} rad/s/$\sqrt{\text{Hz}}$ at 10 Hz. The polarisation cross-coupling, on the other hand, has risen sharply relative to the simple configuration, reaching levels comparable to the CRB floor. This increase is a direct consequence of the broadband ASE source. Whilst the wide spectral bandwidth is essential for the Lyot depolariser to function, it simultaneously increases the rate at which different spectral components accumulate different polarisation states across the coil, enhancing the instantaneous cross-coupling noise amplitude even as its long-term average is stabilised. The thermo-optic fibre noise, by contrast, has been reduced to $\sim 10^{-9}$ rad/s/$\sqrt{\text{Hz}}$ across the entire band of interest, a direct consequence of its $1/\sqrt{L}$ dependence and the longer fibre coil. The Optical Kerr effect presents a shallower spectral slope, starting at 10^{-7} rad/s/$\sqrt{\text{Hz}}$ at 10^{-3} Hz and falling below the ET requirement shortly above 1 Hz, consistent with the improved RIN suppression and the estimated one-order-of-magnitude improvement in splitting asymmetry provided by the MIOC Y-junction.

The remaining noise contributions all fall below the ET requirement of 10^{-10} rad/s/$\sqrt{\text{Hz}}$. Shot noise has been reduced to $\sim 10^{-11}$ rad/s/$\sqrt{\text{Hz}}$ across the full bandwidth, driven by the increased Sagnac sensitivity of the longer fibre coil, despite the accompanying reduction in optical power at the photodetector due to fibre attenuation. The TIA thermal noise sits almost one order of magnitude below the shot noise floor; as the detected optical power decreases with increasing fibre length, the transimpedance gain must be raised to maintain the same voltage swing at the FPGA input, which directly reduces the referred input noise of the amplifier. The Shupe effect reaches $\sim 10^{-12}$ rad/s/$\sqrt{\text{Hz}}$, suppressed by 3–4 orders of magnitude relative to the unmitigated case through the geometric cancellation of the quadrupole winding pattern. Finally, the Faraday effect, already very low in the simple configuration, is further attenuated by the μ-metal housing and falls well below the ET requirement with a $1/f$ spectral dependence across the entire band.

4.2 Evaluation

4.2.1 Comparison with Inertial Sensors

The noise budget presented in the previous section shows the final FOG architecture noise floor, which is of $\sim 10^{-6}$ rad/s/$\sqrt{\text{Hz}}$ in the band of interest between 10 mHz and 1 Hz, is still far from the ET requirement of 10^{-10} rad/s/$\sqrt{\text{Hz}}$. However, it is convenient to put into context this performance compared to the inertial sensor technologies reviewed in section 2.1.2, since the contrast reveals both the strengths of the FOG approach and the specific areas where further development is most critical.

The most direct competitor in the low-frequency band is the beam balance family. Specifically, the best representative, the Cylindrical Rotation Sensor from the University of Washington, which achieves 0.2nrad/$\sqrt{\text{Hz}}$ above 100 mHz and 1 nrad/$\sqrt{\text{Hz}}$ above 30 mHz, with a resonance frequency of 17 mHz. The current FOG noise budget does not yet compete with this performance in absolute terms. However, two structural advantages of the FOG must be highlighted. First, the FOG transfer function is flat from DC, described by the Sagnac equation, presenting no resonance frequency or roll-off, whereas the beam balance sensitivity falls as f^2 below its resonance, placing its lower operational limit closely to the limit of the ET isolation bandwidth. Second, the FOG is intrinsically insensitive to translational motion through the Sagnac effect. The beam balance requires an extraordinarily precise alignment of the centre of mass to the pivot point, typically within tens of nanometres, to suppress the tilt-horizontal coupling below acceptable levels when most of the current prototypes stand above 1 μm. The FOG therefore offers a more robust and frequency-uniform sensing principle, even if its current noise floor requires further research and noise-mitigation implementations.

Regarding optical sensors, the commercial BlueSeis-3A, the highest-resolution commercially available FOG, presents a self-noise of 2×10^{-8} rad/s/$\sqrt{\text{Hz}}$ between 10 mHz and 100 Hz. The custom architecture developed in this thesis sits two orders of magnitude above with the best commercial FOG in the market, but stills shows a great potential.

4.2.2 Comparison with the ET Requirements

The ET active isolation platform requires a rotation sensor with a noise floor of 10^{-10} $rad/s/\sqrt{Hz}$ between 10 mHz and 1 Hz to enable two orders of magnitude of seismic isolation below 1 Hz. The final FOG architecture presented in this thesis does not meet the targeted requirements by approximately four orders of magnitude, with the noise floor dominated by RIN and CRB throughout the entire band of interest. This gap is significant, but it should not be read as a failure of the approach. The analysis conducted across this work shows that the Sagnac principle is well suited to the problem, the dominant noise mechanisms are clearly identified, and further mitigation is possible, according to the literature.

By further applying mitigation strategies for the RIN and the Rayleigh backscattering, the noise levels can decrease significantly, leaving for evaluation the acousto-optic effect and the polarisation cross coupling. The later can be considerably reduced by affordable modern strategies such as the implementation of polarisation maintaining fibre or polarisation scramblers. Considering the ET platforms conditions, the sensor would greatly benefit for the active and passive seismic isolation towards the acousto-optic noise, which needs to be carefully characterised. Then, polarisation cross coupling can be severely reduced by implementing polarisation maintaining fibre at the cost of optical power and monetary cost. These approaches, properly evaluated, would already push down noises below the levels of the best commercial FOG across all the bandwidth of interest. Therefore, the remaining distance to meeting the ET requirements is essentially an engineering challenge, not a fundamental one, exhibiting great potential of improvement.

Chapter 5

Conclusions and perspectives

This chapter gathers the main conclusions drawn from the work carried out, reflecting on the degree to which the original objectives were met, and outlining the directions that future development of this instrument should take. The perspectives section also collects a number of improvement paths that emerged naturally during the project but fell outside its scope, and which are left here as a reference to continue this line of work.

5.1 Conclusions

This thesis was carried out to investigate the development of a custom fibre optic gyroscope that could be designed to meet the rotational sensing requirements of the Einstein Telescope active isolation platform, targeting a noise floor of 0.1–10 $nrad/s/\sqrt{Hz}$ between 10 mHz and 1 Hz. The work began with a structured review of the sensing technologies currently available for tilt measurement at low frequencies, covering mechanical and MEMS gyroscopes, the inertial beam balance sensors, ring laser gyroscopes and fibre optic gyroscopes. From that review, the FOG was selected as the most suitable and highest potential candidate, primarily based on its flat transfer function from DC, its inherent insensitivity to translational motion through the Sagnac effect, and its superior flexibility and robustness compared to ring laser implementations.

The design process was structured as a progressive evolution from the simplest functional FOG architecture toward a refined final configuration. Starting from the simplest operational system consisting of an optical source, a coupler, a fibre coil and a photodetector, each noise mechanism and significant issue was introduced, analysed and addressed in turn. Considering the research done, the phase modulator integrated into the MIOC resolves the sign ambiguity and low-sensitivity problem at near-zero rotation rates. The substitution of the narrowband laser by a broadband ASE source suppresses Coherent Rayleigh Backscattering by several orders of magnitude and simultaneously mitigates the Optical Kerr Effect through the incoherent photon statistics of the source. The Lyot depolariser controlled polarisation fading and partially cross-coupling inside the coil. The quadrupole winding pattern provided geometric cancellation of the Shupe effect and acousto-optic noise. The optical isolator and circulator protected the source and recovered the optical power at the detection stage. Finally, the reference photodetector enables the RIN mitigation and, then, digital processing in the FPGA addresses the data acquisition and leads the modulation of the signal at the MIOC.

The resulting noise budget shows that the final architecture achieves a theoretical noise floor of approximately $10^{-6} rad/s/\sqrt{Hz}$ across the band of interest, dominated by residual RIN and Coherent Rayleigh Backscattering. This result sits four orders of magnitude above the ET requirement, but it represents a great potential through a configuration with still a lot of room to improve, confirming that the large custom coil approach is the correct path forward. The Sagnac scale factor achieved with a 2.5 m diameter coil and 20 km of fibre, $KS = 6.7610^5$ $rads/rad$, demonstrates the sensitivity is a meaningful advantage that a purpose-built instrument can offer over commercial solutions constrained by packaging requirements. Furthermore, many noise contributions were successfully pushed below or close to the ET requirement, validating the architectural choices made throughout the design process. Therefore, the work meets its primary objective: to produce a well-grounded and technically detailed FOG design, supported by a complete noise budget, that establishes a credible foundation for future experimental development.

5.2 Perspectives

The development of this instrument naturally opened more questions. Many areas of improvement, refinement and deeper characterisation were identified along the way but could not be pursued within the scope of this project. They are collected here, together with the improvements that the noise budget most directly motivates, as a reference for the next stages of this work.

5.2.1 Possible Improvements

The noise budget of the final configuration points clearly to where future effort should be directed. The improvements can be grouped into three areas: reducing the dominant noise sources, finding the optimal coil parameters, and addressing the additional instrumental contributions that were not fully characterised in this work.

Further reduction of the main noises

RIN and CRB remain the two dominant contributors across the full band of interest, and both are tied to the residual coherence of the optical source and to imperfections in the common-mode rejection. The 30–40 dB RIN suppression estimated for the reference subtraction scheme assumes good delay matching and stable normalisation, which in practice requires careful characterisation of the optical path delay and of the attenuation difference between the two arms. Active stabilisation of the source output power through a feedback loop acting on the pump current of the gain medium would provide an additional layer of suppression. For CRB, selecting a source with a wider spectral bandwidth than the 33 nm assumed here, or shaping the ASE emission profile to reduce its effective coherence length, would proportionally push this noise further down [38].

Polarisation cross-coupling has also emerged as a significant contributor in the final configuration, a direct side effect of the broadened source spectrum needed to make the Lyot depolariser work. A fully polarisation-maintaining coil architecture could address this, though the splice losses and propagation penalties of PMF at these fibre lengths would need to be weighed carefully against the gain.

Optimal fibre coil evaluation

A subtlety that the noise budget of this thesis highlights is that fibre length is not a free parameter to be maximised without constraint. Increasing L simultaneously raises the Sagnac scale factor, which reduces all noise contributions when referred to rotation units, but it also increases the thermo-optic fibre noise and the fibre attenuation, reducing the optical power at the photodetector and raising the shot noise floor. The optimal fibre length is therefore the one that minimises the total noise at the photodetector, balancing these competing trends. A dedicated optimisation study could sweep L for a fixed coil diameter and source power, evaluating each noise term from the equations developed in Chapter 3. This would identify the length at which the shot noise and thermo-optic noise are comparable in magnitude, thereby revealing the global minimum of the noise floor. Based on the expressions derived in this work, this optimum is expected to lie significantly above the 20 km assumed in the final configuration, but the precise value depends on the attenuation coefficient of the chosen fibre and the available source power, and it should be determined numerically as a first step in the next design iteration.

Further instrumental noises and reliability

Beyond the dominant optical noise terms, a complete characterisation of the instrument requires addressing several noise and uncertainty contributions that were not fully modelled in this work and which could become the limiting floor once the RIN and CRB are suppressed.

Several noise contributions were not fully modelled in this work and could become relevant once the dominant terms are suppressed. The FPGA phase modulation chain carries its own electrical noise, which translates into spurious phase shifts indistinguishable from a Sagnac signal, and its spectral purity within the isolation bandwidth needs to be characterised explicitly. ADC dynamic range and bit depth set a quantisation noise floor that must be considered carefully in the noise budget. Optical splices and connectors contribute insertion loss and residual polarisation cross-coupling, whose cumulative effect across the full signal path can degrade the effective extinction ratio below the values achievable with individual components. Wavelength drift of the ASE source introduces a slow scale factor error that, inside a closed feedback loop, is indistinguishable from a low-frequency rotation signal and must be controlled through temperature stabilisation and periodic [36].

On the thermal side, the Shupe model assumed smooth and slowly varying gradients, which may not hold in the mechanical environment of an active isolation platform. As well, winding patterns do not reach perfect geometric symmetry, meaning they are more effective against some spatial gradient distributions than others. Coil potting and thermal strapping of the electronics away from the sensing volume are standard industrial practices that would reduce both the amplitude and the spatial non-uniformity of the thermal fluctuations, directly improving the residual Shupe [17].

These refinements, taken together with many others not explored in this work, define a concrete and realistic roadmap toward the ET noise floor. The meticulous assessment of each noise source, architectural choice and inherent characteristic of the different instruments reveals genuine potential to meet the ET requirements. However, further research, careful experimental validation and the hard lessons of both, theoretical and physical testing, will be required to achieve this goal.

Bibliography

[1] Robert Naeye : Detection of gravitational waves heralds new era of science, 2 2016.

[2] Alexandre Le Tiec : A monochromatic gravitational wave of pulsation $\omega = 2\pi/t$ propagates along the z axis. ResearchGate figure. Accessed June 2026.

[3] GWoptics : Einstein telescope optical layout. Online resource, 2021.

[4] Andreas Brotzer, Heiner Igel *et al.* : Characterizing the background noise level of rotational ground motions on earth. *Seismological Research Letters*, 2023.

[5] Havana Paris : Horizontal inertial sensor response to translation and tilt. ResearchGate. Accessed June 2026.

[6] James McCann : Low frequency ground rotation sensors for advanced gravitational wave detectors. Mémoire de D.E.A., University of Western Australia, 2021. Verify institution and thesis type from PDF.

[7] Michael P. Ross *et al.* : A vacuum-compatible cylindrical inertial rotation sensor with picoradian sensitivity. 2023.

[8] Anthony Lawrence : *Modern Inertial Technology: Navigation, Guidance, and Control*. Springer-Verlag, New York, 2 édition, 1998.

[9] LioCrebifx : Fibre optic gyro working principle, n.d. Accessed: 2026-06-09.

[10] Silvano Donati : *In Fotorivelatori*. AEI, Milano, 1997. Capítulo correspondiente al archivo 2c.pdf; completar título y páginas.

[11] Anthony Lawrence : *Modern Inertial Technology: Navigation, Guidance, and Control*. Mechanical Engineering Series. Springer, 2 édition, 1998.

[12] C. Caucheteur, S. Bette, F. Lhommé, K. Chah, M. Wuilpart, M. Blondel et P. Mégret : Numerical reconstruction of induced birefringence in uniform fiber bragg gratings through polarization properties measurement. *In Proceedings of SPIE/Conference on Fiber Bragg Gratings*, 200X. Exact year/venue to be completed.

[13] DK Photonics : Optical circulator application, n.d. Accessed: 2026-06-09.

[14] Edmund Optics : 10 x 10 mm aperture quartz lyot depolarizer, n.d. Accessed: 2026-06-09.

[15] X. Li, Y. Wang, J. Liu *et al.* : Technical drawing of mioc structure (figure 2), 2021. Accessed: 2026-06-09.

[16] Ruifeng Yang; Shuangchao Ge; Bin Li; Chenxia Guo : Analysis of fiber-optic coil shupe effect for different fiber coil winding structure and winding processes optimization.

[17] Jérémie Pillon et collaborators : Thermomechanical analysis of the effects of homogeneous thermal field induced in the sensing coil of a fiber-optic gyroscope. *Optics & Laser Technology*, 153:108266, 2022.

[18] Tucsen Photonics : Photon shot noise in scientific imaging: Snr, n.d. Accessed: 2026-06-09.

[19] Quantifi Photonics : Relative intensity noise (rin) in optical systems. Rapport technique Application Note v1.1, Quantifi Photonics, 2022. Accessed: 2026-06-09.

[20] Anthony Bercy : Personal communication, avril 2026. MAAGM partner contribution, Figure 3.17.

[21] Sumeet Kulkarni et Jessie Thwaites : Guide to gravitational waves. `https://astrobites.org/2023/11/08/guide-to-gravitational-waves/`, novembre 2023. Astrobites. Accessed: June 2026.

[22] Particle Physics Group, University of Antwerp : The Einstein Telescope. `https://www.uantwerpen.be/en/research-groups/particle-physics-group/research/gravitational-waves/einstein-telescope/`, 2024. Accessed: June 2026.

[23] Lucia Trozzo et Francesca Badaracco : Seismic and Newtonian noise in the GW detectors. *Galaxies*, 10(1):20, janvier 2022.

[24] Gilles Magain : H-infinity robust controller development for seismic isolation of gravitational-wave detectors: Implementation on the E-TEST prototype. Master's thesis, Université de Liège, Faculté des Sciences appliquées, 2025. Supervisors: Christophe Collette, Pierre Sacré. Available at `https://matheo.uliege.be/handle/2268.2/23384`.

[25] Wikibooks Contributors : Control systems: Feedback loops. Wikibooks. Accessed June 2026.

[26] Jens Havskov et Gerardo Alguacil : Seismic sensors. *In Instrumentation in Earthquake Seismology*, pages 13–100. Springer, Cham, 2016.

[27] Fabrice Matichard et Matthew Evans : Review: Tilt-free low-noise seismometry. *Bulletin of the Seismological Society of America*, 105(2):497–510, 2015.

[28] Vittorio M. N. Passaro, Antonello Cuccovillo, Lorenzo Vaiani, Martino De Carlo et Carlo Edoardo Campanella : Gyroscope technology and applications: A review in the industrial perspective. *Sensors*, 17(10):2284, octobre 2017.

[29] E. Calloni, Archimedes Collaboration et Virgo Collaboration : High-bandwidth beam balance for vacuum-weight experiment and Newtonian noise subtraction. *The European Physical Journal Plus*, 136(3):335, mars 2021.

[30] Krishna Venkateswara, Jerome Paros, Paul Bodin, William Wilcock et Harold J. Tobin : Rotational seismology with a Quartz Rotation Sensor. *Seismological Research Letters*, 93(1):173–180, 2022.

[31] V. Yusuf Şenyürek H. Selçuk Varol : Low cost fiber optic angular velocity sensor. Technical document. Verify author, year and title from PDF.

[32] J. Mlynek C.S. Adams, O. Carnal : Atom interferometry. *In Atom Interferometry*. McGraw–Hill, 5 édition, 1994. Likely source of ScienceDirect chapter S1049250X08600737; verify exact chapter.

[33] Felix Bernauer, Joachim Wassermann, Frederic Guattari, Arnaud Frenois, Alexandre Bigueur, Arnaud Gaillot, Elliot de Toldi, Damien Ponceau, Ulrich Schreiber et Heiner Igel : Blueseis3a: Full characterization of a 3c broadband rotational seismometer. *Seismological Research Letters*, 89(2A):620–629, 2018.

[34] Awad Samir Gerges : *Novel fibre-optic-based interferometric sensors exploiting coherent and low-coherence signal processing techniques.* Thèse de doctorat, University of Kent, 1990.

[35] Sander Konijnenberg, Aurèle J. L. Adam et H. Paul Urbach : 5.10: Fringe visibility, 2024. Accessed: 2026-06-09.

[36] Hervé C. Lefèvre : The fiber-optic gyroscope: Challenges to become the ultimate rotation-sensing technology. *Optical Fiber Technology*, 19(6):828–832, 2013.

[37] Cronologic GmbH : Rayleigh scattering, n.d. Accessed: 2026-06-09.

[38] C. C. Cutler *et al.* : Rayleigh backscattering in a fiber gyroscope with limited coherence sources. *Journal of Lightwave Technology*, LT-1(2):381–387, 1983.

[39] Xiaoping Zhang, Wei Li, Yixin Wang et Jian Liu : Theoretical analysis on coherent noise by rayleigh backscattering in bidirectional transmission system with single mode fiber. *In Proceedings of the 2009 International Forum on Information Technology and Applications (IFITA)*, volume 1, pages 225–228, 2009.

[40] Grokipedia : Physics of optical holography, n.d. Accessed: 2026-06-09.

[41] NKT Photonics : Koheras ADJUSTIK – single-frequency fiber lasers. https://www.nktphotonics.com/products/single-frequency-lasers/koheras-adjustik/, 2026. Accessed: June 2026.

[42] OZ Optics Ltd. : ASE flat spectrum C-band module – OEM. https://www.ozoptics.com/news/pr_208.html, mai 2021. Press release. Accessed: June 2026.

[43] Yong Sheng Ong : Optical fiber sensor system design utilizing the field programmable gate array. *In 2017 IEEE SENSORS*. IEEE, 2017.

[44] RP Photonics Consulting GmbH : Shot noise, n.d. Accessed: 2026-06-09.

[45] Texas Instruments : Op amp noise theory and applications. Rapport technique SBOA060, Texas Instruments, 2000. Accessed: 2026-06-09.

[46] Yiqiu Ma, Haixing Miao, Chunnong Zhao, Stefan L. Danilishin, Yanbei Chen et David G. Blair : Quantum noise in optical interferometers. *Physical Review A*, 86(2):023817, 2012.

[47] Frédéric Guattari, Stéphane Chouvin, Cédric Moluçon et Hervé C. Lefèvre : A simple optical technique to compensate for excess RIN in a fiber-optic gyroscope. *In 2014 DGON Inertial Sensors and Systems (ISS)*, pages 1–14, Karlsruhe, Germany, septembre 2014. IEEE.

[48] RP Photonics Consulting GmbH : Relative intensity noise, n.d. Accessed: 2026-06-09.

[49] RP Photonics Consulting GmbH : Photocurrent, n.d. Accessed: 2026-06-09.

[50] Rodrigo Acuna Herrera, Chiu Tai Law, Arash Mafi : Calculation of the acousto-optic coupling coefficients in optical fibers, 2013. Accessed: 2026-06-09.

[51] Pedja Mihailovic et Slobodan Petricevic : Fiber optic sensors based on the Faraday effect. *Sensors*, 21(19):6564, 2021. Published 30 Sep 2021.

[52] Sabina Merlo, Michele Norgia et Silvano Donati : Fiber gyroscope principles. *In* José Miguel López-Higuera, éditeur : *Handbook of Fibre Optic Sensing Technology*, chapitre 16. John Wiley & Sons, Chichester, 2000.

[53] S. Huang, L. Thévenaz, K. Toyama, B. Y. Kim et H. J. Shaw : Optical Kerr-effect in fiber-optic Brillouin ring laser gyroscopes. *IEEE Photonics Technology Letters*, 5(3):365–367, mars 1993.